Physics Reports 534 (2014) 1–37

Contents lists available at ScienceDirect

Physics Reports

journal homepage: www.elsevier.com/locate/physrep

Numerical simulations of time-resolved quantum electronics

Benoit Gaury, Joseph Weston, Matthieu Santin, Manuel Houzet, Christoph Groth, Xavier Waintal*

CEA-INAC/UJF Grenoble 1, SPSMS UMR-E 9001, Grenoble F-38054, France

ARTICLE INFO

Article history:
Accepted 9 September 2013
Available online 20 September 2013
editor: G.E.W. Bauer

ABSTRACT

Numerical simulation has become a major tool in quantum electronics both for fundamental and applied purposes. While for a long time those simulations focused on stationary properties (e.g. DC currents), the recent experimental trend toward GHz frequencies and beyond has triggered a new interest for handling time-dependent perturbations. As the experimental frequencies get higher, it becomes possible to conceive experiments which are both time-resolved and fast enough to probe the internal quantum dynamics of the system. This paper discusses the technical aspects – mathematical and numerical – associated with the numerical simulations of such a setup in the time domain (i.e. beyond the single-frequency AC limit). After a short review of the state of the art, we develop a theoretical framework for the calculation of time-resolved observables in a general multiterminal system subject to an arbitrary time-dependent perturbation (oscillating electrostatic gates, voltage pulses, time-varying magnetic fields, etc.) The approach is mathematically equivalent to (i) the time-dependent scattering formalism, (ii) the time-resolved non-equilibrium Green's function (NEGF) formalism and (iii) the partition-free approach. The central object of our theory is a wave function that obeys a simple Schrödinger equation with an additional source term that accounts for the electrons injected from the electrodes. The time-resolved observables (current, density, etc.) and the (inelastic) scattering matrix are simply expressed in terms of this wave function. We use our approach to develop a numerical technique for simulating time-resolved quantum transport. We find that the use of this wave function is advantageous for numerical simulations resulting in a speed up of many orders of magnitude with respect to the direct integration of NEGF equations. Our technique allows one to simulate realistic situations beyond simple models, a subject that was until now beyond the simulation capabilities of available approaches.

Contents

1. Introduction 2
   1.1. From AC quantum transport to voltage pulses and "electronic quantum optics" 4
   1.2. Numerical simulations of time-resolved quantum transport 4
2. Generic model for time-dependent mesoscopic devices 5
3. Non-equilibrium Green's function (NEGF) approach 5
   3.1. Equations of motion for the Retarded (G^R) and Lesser ($G^<$) Green's functions 6
   3.2. Equations of motion for lead self-energies 6
4. Wave function (WF) approach 7
   4.1. Construction of the wave function 7
   4.2. Effective Schrödinger equation 8

* Corresponding author. Tel.: +33 0438786968.
E-mail address: xavier.waintal@cea.fr (X. Waintal).

0370-1573/$ – see front matter © 2013 Elsevier B.V. All rights reserved.
http://dx.doi.org/10.1016/j.physrep.2013.09.001

5. Time-dependent scattering theory ... 9
5.1. Conducting modes in the leads ... 9
5.2. Construction of the scattering states ... 9
5.3. Connection to the wave function approach ... 10
5.4. Generalization of the Fisher–Lee formula ... 10
5.5. Link with the partition-free initial condition approach ... 11
5.6. "Floquet wave function" and link with the Floquet scattering theory ... 11
6. Strategies for efficient numerical simulations ... 12
6.1. GF-A: brute-force integration of the NEGF equations ... 12
6.2. GF-B: Integrating out the time-independent subparts of the device ... 13
6.3. GF-C: integration scheme that preserves unitarity ... 14
6.4. WF-A: direct integration of Eq. (27) ... 14
6.5. WF-B: subtracting the stationary solution, integration of Eq. (31) ... 15
6.6. WF-C: from integro-differential to differential equation ... 15
6.7. WF-D: faster convergence using the wide band limit ... 15
7. Numerical test of the different approaches ... 16
7.1. Green's function based algorithms ... 16
7.2. Wave functions based algorithms ... 16
7.3. Relative performance of the different approaches ... 18
8. A Landauer formula for voltage pulses ... 19
8.1. Total number of injected particle ... 19
8.2. Scattering matrix of a voltage pulse ... 19
8.3. Voltage pulses in multiterminal systems ... 21
8.4. A comment on the electrostatics ... 22
9. A pedestrian example: propagation and spreading of a voltage pulse inside a one dimensional wire ... 23
9.1. Scattering matrix: analytics ... 24
9.2. Scattering matrix: numerics ... 25
9.3. Spreading of a voltage pulse inside a one dimensional wire: analytics ... 26
9.4. Spreading of a voltage pulse inside a one dimensional wire: numerics ... 27
10. A two dimensional application to a flying Qubit ... 30
10.1. Integral over energies ... 30
10.2. Model ... 30
10.3. Time-resolved simulations ... 31
11. Conclusion ... 32
Acknowledgments ... 33
Appendix A. Understanding the origin of the "source" term and "memory" kernel ... 34
Appendix B. Derivation of the path integral formula (68) ... 34
Appendix C. Various analytical results for Green's functions of the 1d chain ... 35
References ... 36

1. Introduction

The last ten years have seen the development of an increasing number of finite frequency low temperature nanoelectronic experiments in the GHz range and above. As the frequencies get higher, they become larger than the thermal background (1 GHz corresponds to 50 mK) and eventually reach the internal characteristic frequencies of the system. Conceptually new types of experiments become possible where one probes directly the internal quantum dynamics of the devices. Beside a large interest for setups with very few degrees of freedom (e.g. Qubits), open systems with continuous spectra – the subject of the present paper – have been studied comparatively little. Experiments performed in the time domain are even more recent.

This article is devoted to the development of the theoretical apparatus needed to build efficient numerical techniques capable of handling the simulation of nanoelectronic systems in the time domain. While the theoretical basis for such a project are, by now, well established, neither of the two (equivalent) standard approaches – the time-dependent Non-equilibrium Green's function [1] (NEGF) and the time-dependent scattering formalism [2] – are, in their usual form, well suited for a numerical treatment. Here we show that a third – wave-function based – approach, mathematically equivalent to both NEGF and scattering theory, naturally leads to efficient numerical algorithms.

The wave function approach followed here has a simple mathematical structure: we consider a generic infinite system made of several semi-infinite electrodes and a central mesoscopic region as sketched in Fig. 1. Introducing the wave function $\Psi_{\alpha E}(\vec{r}, t)$ which depends on space $\vec{r}$ and time t as well as on the injection energy E and mode α, we find that it obeys a Schrödinger equation with an additional source term:

$$i\hbar\frac{\partial}{\partial t}\Psi_{\alpha E}(\vec{r}, t) = H(t)\Psi_{\alpha E}(\vec{r}, t) + \sqrt{v_\alpha}\xi_{\alpha E}(\vec{r})e^{-iEt/\hbar}, \tag{1}$$

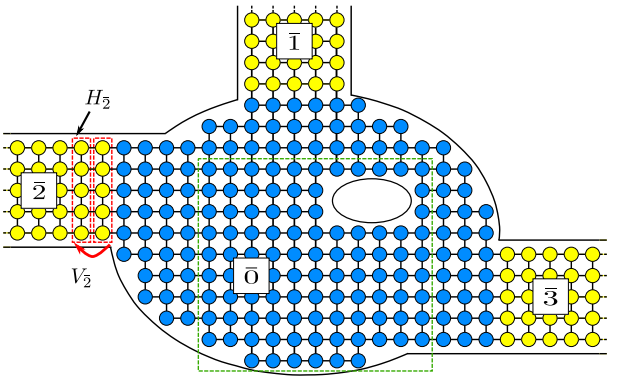

Fig. 1. Sketch of a generic multiterminal system where the central part $\bar{0}$ (blue circles) is connected to three semi-infinite leads $\bar{1}$, $\bar{2}$, $\bar{3}$ (yellow circles). The leads are kept at equilibrium with temperature $T_{\bar{m}}$ and chemical potential $\mu_{\bar{m}}$. The dashed green line indicates a region that will be integrated out in Fig. 2. (For interpretation of the references to color in this figure legend, the reader is referred to the web version of this article.)

where $H(t)$ is the time-dependent (one-particle) Hamiltonian of the system while $\xi_{\alpha E}(\vec{r})$ corresponds to the transverse wave function of the conducting channel α at the electrode-device interface (the number α is labeling both the different channels and the electrodes to which they are associated) and v_α is the associated mode velocity. The various observables are then easily expressed in terms of this wave function. For instance, the particle current density (without electro-magnetic field) reads:

$$\vec{I}(\vec{r},t) = \mathrm{Im}\sum_\alpha \int \frac{dE}{2\pi}\, \Psi^*_{\alpha E}(\vec{r},t)\vec{\nabla}\Psi_{\alpha E}(\vec{r},t) f_\alpha(E) \tag{2}$$

where $f_\alpha(E)$ is the Fermi function in the electrode of channel α. The source term and mode velocities in Eq. (1) are standard objects of the theory of stationary quantum transport and are readily obtained while Eq. (1) itself can be integrated numerically (as a function of time) without difficulty. The observables are obtained in a second step by integrating Eq. (2) over the incident energy. Eqs. (1) and (2) thus form a simple set of equations in the mixed time-energy domain, easily amenable to numerical evaluations. Note that a treatment of the electron–electron interactions at the mean field level implies that these two equations become linked: for instance the Hartree potential is a function of the time-resolved local electron density. Hence, by introducing self-consistent potentials, these techniques can be easily extended to include electron–electron interactions at the mean field level (including time-dependent density functional theory). As such a treatment is essentially independent from the non-interacting aspects discussed here, the link with the electrostatic, or more generally electron–electron interactions, will be mostly ignored in the remaining of this article (except in the discussion of Section 8.4).

This article is structured as follows. After a short survey of the literature on time-resolved quantum transport with a focus on numerical work, this article starts with the construction of the theory of time-dependent transport with an emphasis on drawing connections between the various possible approaches. We discuss our general model (Section 2) and the basic equations of the NEGF formalism (Section 3) and then proceed in Section 4 with the introduction of the time-dependent wave function as a mathematical artifact to reformulate the NEGF formalism. Section 5 is devoted to a constructive presentation of the scattering approach. We show that it is strictly identical to the wave function of Section 4. We also find that the NEGF approach is equivalent to the partition-free approach introduced in [3] and further developed in Ref. [4]. This concludes the formalism part of this work. The next sections leverage on the previous ones to build efficient numerical techniques for the simulation of time-resolved transport. Section 6 discusses (seven) different practical algorithms that can be used to simulate time-dependent transport. Section 7 presents some numerical results that illustrate the strengths and weaknesses of the approaches of Section 6. We eventually converge toward a very simple algorithm (later referred to as WF-D) which is many orders of magnitude faster than the direct NEGF approach (yet mathematically equivalent). The reader is referred to Table 1 for a quick glance at the relative speeds of the different approaches. In the last part of this article, we restrict the theory (so far valid for an arbitrary form of the time-dependent perturbation) to the particular case where a voltage pulse is applied to one of the electrodes. Section 8 is devoted to a derivation of the voltage pulse analogue to the Landauer formula for DC transport. In Section 9 we apply the formalism to a very simple situation: the propagation and spreading of a voltage pulse in a one dimensional wire. This application, for which both analytical and numerical results can be obtained, serves to build our physical understanding of the physics of fast pulses. We end this article with Section 10 where we present some simulations of a flying Qubit inspired from recent experiments performed in a two-dimensional electron gas [5].

We end this introduction with a short review of the literature on the simulations of time-resolved quantum transport. Although we briefly mention AC transport, the focus will be on situations where the perturbation is localized in time. Also, the emphasis is on techniques that are suited to numerical treatments.

1.1. From AC quantum transport to voltage pulses and "electronic quantum optics"

The history of AC quantum transport probably starts in the 60s with the prediction and measurement of the photo assisted tunneling [6], an effect that has attracted some renewed attention recently in the context of noise measurements [7]. Around the same time was the discovery of the AC Josephson effect [8] between two superconductors. Other early experiments showed that it was possible to pump current in a mesoscopic device using the Coulomb blockade effect [9] or, more recently, the quantum modulation of the wave function [10,11].

An important point that was recognized early by Büttiker and his collaborators is that a proper treatment of the electrostatics of the system was crucial when dealing with finite frequency quantum transport [12–16]. Indeed, in non-interacting AC theory, the electronic density fluctuates with time and space and as a result the current is no longer a conserved quantity. Allowing for the extra charges to be screened by nearby conductors restores the neutrality of the global system, as well as current conservation once the displacement currents are properly included. One finds that it is difficult to observe the internal time scales of a device as they are often hidden by the classical RC time. One of the most spectacular predictions of this theory [12,14] is that the resistance R that sets the RC time of a "quantum capacitor" (a quantum dot connected to one electrode and capacitively coupled to a gate) is given by half the resistance quantum $h/(2e^2)$ irrespective of the actual resistance of the constriction that forms the "R" part of the device. The experimental verification of this prediction [17] was a salient feature in the field of AC quantum physics. More recent experiments include the measurement of a quantum LC circuit [18], the statistics of the emitted photons [19,20] and the control of shot noise using multiple harmonics [21].

The theory of those AC quantum transport effects has now evolved into a field in itself which lies outside the scope of this short discussion. We refer to [22] for an introduction to the (Floquet) scattering theory and to [23] for the numerical aspects. Refs. [24–26] discuss practical aspects associated with developing schemes that preserve gauge invariance and charge conservation. Recent developments on the numerical side may be found in [27] while the emerging topic of Floquet topological insulators is reviewed in [28].

Time-resolved quantum transport is not, *a priori*, very different from AC quantum transport. A series of seminal works on time-resolved quantum electronics showed however that the current noise associated with voltage pulses crucially depends on their actual shape (i.e. on the details of the harmonics contents and of the relative phases of the various harmonics) [29,30]. More precisely, Levitov and collaborators found that pulses of Lorentzian shape can be noiseless while other shapes are associated with extra electron–holes excitations that increase the noise of the signal. It was predicted that Lorentzian pulses could form noiseless single electron sources that could be used in quantum devices such as flying Qubits. These predictions are the object of an intensive experimental activity [31,32]. Meanwhile, other experiments looked for various ways to construct coherent single electron sources and reproduce known quantum optics experiments with electrons, a program sometimes referred to as "electronic quantum optics". Ref. [33] used a small quantum dot to make such a source [34–38] which was later used in [39] to perform an electronic Hong–Ou–Mandel experiment. A similar source, yet working at much larger energy has been recently demonstrated in [40]. Another route [41,42] used SAW (Surface Acoustic Waves) to generate a propagating confining potential that transports single electrons through the sample. These experiments are mostly performed in two dimensional gasses made in GaAs/GaAlAs heterostructures whose rather small velocities (estimated around 10^4–10^5 m s^{-1} in the quantum Hall regime) and large sizes (usually several μm) make experiments in the GHz range possible. Smaller devices, such as carbon nanotubes, require the use of frequencies in the THz range. Although THz frequencies are still experimentally challenging, detection schemes in these range have been reported recently [43].

1.2. Numerical simulations of time-resolved quantum transport

While simulations of the time-dependent Schrödinger equation are almost as old as quantum mechanics itself, time-resolved quantum transport requires that two additional difficulties be dealt with: the statistical physics of the many-body problem (whose minimum level is to include the Pauli principle and the thermal equilibrium of the leads) and the fact that quantum transport takes place in *infinite* systems. Early numerical simulations of time-resolved quantum transport were based on a seminal paper by Caroli, Combescot, Nozières, and Saint-James [44] which sets the basis of the NEGF formalism (itself based on the Keldysh formalism [45]) in a one dimensional situation. This formalism was used in [46] to study resonant tunneling of a single level. The formalism for a generic mesoscopic system was established by Jauho, Wingreen and Meir [1,47] extending the stationary formalism put forward by Wingreen and Meir [48] which itself extends the original work of [44]. The time-dependent NEGF approach described in these papers is still the basis of most numerical works (while the scattering theory is perhaps more favored for analytical calculations). Considering that the formalism is 25 years old, the number of publications on the subject is rather small. This is due in part to the fact that it only recently became possible to perform experiments in the relevant regimes (i.e. GHz frequencies at dilution fridge temperatures), and also to the extreme computational cost of a direct integration of the NEGF equations. Many recent works describe various strategies for integrating the integro-differential equation of the NEGF formalism, including direct approaches [49–51], a semi analytical approach [52], a parametrization of the analytical structure of the equations [53] and a recursive approach [54]. The important issue of properly dealing with electron–electron interactions has been discussed in [55–58]. Alternative approaches to NEGF include a direct treatment of the one electron density matrix [59] or the use of a "stroboscopic" wave packet basis [60,61]. Perhaps the most advanced alternative to NEGF is the partition-free approach

introduced by Cini [3] in the early 80s. In this approach, instead of "integrating out" the electrodes' degrees of freedom, as it is done in NEGF, one starts with the exact density matrix at equilibrium at $t = 0$ and follows the system states as they are driven out of equilibrium by the time-dependent perturbation. This approach can be followed with Green's functions [62, 63] or more conveniently directly at the wave function level [4,64,65].

To the best of our knowledge, the best performance so far has been obtained with the partition-free approach where around 100 sites could be studied (the direct NEGF simulations are usually confined to 10 sites or fewer). The wave function approach leverages the fact that calculations of the electric current do not require all of the information contained within Green's functions. Nevertheless, all these techniques suffer from the fact that the systems are intrinsically infinite which brings non local (in time) terms into the dynamical equations. An interesting approach followed in Ref. [63] consists of ignoring these non local terms and considering a large finite system instead.

In the rest of this article, we will revisit in turn the three main approaches discussed above. While our starting point is the NEGF formalism, we shall construct systematically the two other approaches, thereby proving (both at the mathematical and numerical level) the complete equivalence between time-dependent NEGF, scattering theory and the partition-free approach.

2. Generic model for time-dependent mesoscopic devices

We consider a quadratic discrete Hamiltonian for an open system

$$\hat{\mathbf{H}}(t) = \sum_{i,j} \mathbf{H}_{ij}(t) c_i^\dagger c_j \tag{3}$$

where $c_i^\dagger$ (c_j) are the usual Fermionic creation (annihilation) operators of a one-particle state on site i. The site index i includes all the degrees of freedom present in the system, i.e. space but also spin, orbital (s,p,d,f) and/or electron/hole (superconductivity), so that a large number of situations can be modeled within the same framework. The system consists of a central region, referred to as $\bar{0}$ connected to M semi-infinite leads labeled $\bar{1}\ldots\bar{M}$ as depicted in Fig. 1. $\mathbf{H}(t)$ is formally an infinite matrix and can be viewed as consisting of sub-blocks $\mathbf{H}_{\bar{m}\bar{n}}$.

$$\mathbf{H} = \begin{pmatrix} \mathbf{H}_{\bar{0}\bar{0}} & \mathbf{H}_{\bar{0}\bar{1}} & \mathbf{H}_{\bar{0}\bar{2}} & \ldots \\ \mathbf{H}_{\bar{1}\bar{0}} & \mathbf{H}_{\bar{1}\bar{1}} & 0 & \ldots \\ \mathbf{H}_{\bar{2}\bar{0}} & 0 & \mathbf{H}_{\bar{2}\bar{2}} & \ldots \\ \ldots & \ldots & \ldots & \ldots \end{pmatrix}. \tag{4}$$

A semi-infinite lead $\bar{m}$ is itself a periodic system where a unit cell is described by a Hamiltonian matrix $H_{\bar{m}}$ which is coupled to the neighboring cells by the coupling matrix $V_{\bar{m}}$:

$$\mathbf{H}_{\bar{m}\bar{m}} = \begin{pmatrix} H_{\bar{m}} & V_{\bar{m}} & 0 & 0 & \ldots \\ V_{\bar{m}}^\dagger & H_{\bar{m}} & V_{\bar{m}} & 0 & \ldots \\ 0 & V_{\bar{m}}^\dagger & H_{\bar{m}} & V_{\bar{m}} & \ldots \\ \ldots & \ldots & \ldots & \ldots & \ldots \end{pmatrix}. \tag{5}$$

While the time dependence of the device region $\mathbf{H}_{\bar{0}\bar{0}}(t)$ can (and will) be arbitrary, the leads are only subject to homogeneous time-dependent voltages so that $\mathbf{H}_{\bar{m}\bar{m}}(t) = w_{\bar{m}}(t) 1_{\bar{m}} + \mathbf{H}_{\bar{m}\bar{m}}(t = 0)$ ($1_{\bar{m}}$ is the identity matrix in lead m). Following standard practice, we perform a unitary gauge transformation $\hat{W} = \exp(-i \sum_{i\in\bar{m}} \phi_{\bar{m}}(t) c_i^\dagger c_i)$ on the Hamiltonian with $\phi_{\bar{m}}(t) = \int_{-\infty}^{t} du\, w_{\bar{m}}(u)$ being the integral of the time-dependent voltage. After the gauge transformation, we recover time-independent Hamiltonians for the leads while the matrix elements that connect the lead to the central part now acquire an time-varying phase:

$$\mathbf{H}_{\bar{m}\bar{0}} \to e^{i\phi_{\bar{m}}(t)} \mathbf{H}_{\bar{m}\bar{0}}. \tag{6}$$

The quantum mechanical aspects being properly defined, we are left to specify the statistical physics; each lead is supposed to remain at thermal equilibrium with a chemical potential $\mu_{\bar{m}}$ and a temperature $T_{\bar{m}}$. Note that the thermal equilibrium condition is most simply expressed for time-independent leads, i.e. after the gauge transformation. This particular choice of boundary condition is significant and its physical meaning will be discussed in more depth later in the text (Section 8).

3. Non-equilibrium Green's function (NEGF) approach

Here we summarize the basic equations of the time-dependent NEGF formalism [48,1] that constitutes the starting point of our approach. We refer to the original [66] or more recent Refs. [23,67] for a derivation of these equations. The basic objects under consideration are the Lesser $\mathcal{G}^<(t, t')$ and Retarded $\mathcal{G}^R(t, t')$ Green's functions of the system,

$$\mathcal{G}_{ij}^R(t, t') = -i\theta(t - t')\langle\{c_i(t), c_j^\dagger(t')\}\rangle\,, \tag{7}$$

$$\mathcal{G}_{ij}^<(t, t') = i\langle c_j^\dagger(t') c_i(t)\rangle\,, \tag{8}$$

where the operator $c_i(t)$ corresponds to c_i in the Heisenberg representation and $\theta(t)$ is the Heaviside function. For a quadratic Hamiltonian, the Retarded Green's function takes a simple form in terms of the "first quantization" evolution operator of the system:

$$\mathcal{G}^R(t,t') = -i\theta(t-t')U(t,t') \tag{9}$$

where the unitary evolution operator $U(t,t')$ verifies $i\partial_t U(t,t') = \mathbf{H}(t)U(t,t')$ and $U(t,t) = 1$.

The physical observables can be written simply in terms of the Lesser Green's function. For instance the particle current between sites i and j reads,

$$I_{ij}(t) = \mathbf{H}_{ij}(t)G^<_{ji}(t,t) - \mathbf{H}_{ji}(t)G^<_{ij}(t,t) \tag{10}$$

while local electron density is $\rho_i(t) = -iG^<_{ii}(t,t)$.

Suppose that one is interested in the quantum propagation of a wave packet $\Psi(t)$ according to the Schrödinger equation $i\partial_t\Psi(t) = \mathbf{H}\Psi(t)$ with an initial condition given by $\Psi(t = t_0) = \Psi_0$. Then one finds that $\Psi(t)$ is simply given by $\Psi(t) = i\mathcal{G}^R(t,t_0)\Psi_0$. In other words, the Retarded Green's function encodes the quantum propagation of a wave packet. The Lesser Green's function, on the other hand, captures the remaining many-body / statistical physics aspects: the Pauli principle, the finite temperature properties of the leads and the fact that the "initial conditions", say an electric voltage pulse, are given in terms of macroscopic quantities (as opposed to an initial microscopic wave packet) and spread over a finite time window.

3.1. Equations of motion for the Retarded (G^R) and Lesser ($G^<$) Green's functions

Introducing the projections of Green's functions on the central region $G^R(t,t') = \mathcal{G}^R_{\bar{0}\bar{0}}(t,t')$ and $G^<(t,t') = \mathcal{G}^<_{\bar{0}\bar{0}}(t,t')$, one can obtain effective equations of motion where the leads' degrees of freedom have been integrated out. The equation of motion for G^R reads [67],

$$i\partial_t G^R(t,t') = \mathbf{H}_{\bar{0}\bar{0}}(t)G^R(t,t') + \int du\ \Sigma^R(t,u)G^R(u,t') \tag{11}$$

or its symmetric counterpart

$$i\partial_{t'} G^R(t,t') = -G^R(t,t')\mathbf{H}_{\bar{0}\bar{0}}(t') - \int du\ G^R(t,u)\Sigma^R(u,t') \tag{12}$$

with the initial condition $\lim_{\tau\to 0} G^R(t+\tau,t) = -i$. The self-energies encapsulate the effect of the leads:

$$\Sigma^R(t,t') = \sum_{\bar{m}=1}^{\bar{M}} \Sigma^R_{\bar{m}}(t,t') \tag{13}$$

with

$$\Sigma^R_{\bar{m}}(t,t') = \mathbf{H}_{\bar{0}\bar{m}}(t)g^R_{\bar{m}}(t,t')\mathbf{H}_{\bar{m}\bar{0}}(t') \tag{14}$$

where $g^R_{\bar{m}}(t,t')$ is the isolated lead Retarded Green's function, i.e. *the surface Green's function of the lead in the absence of coupling to the central region.*

The equation of motion for the Lesser Green's function can be integrated formally and reads [66,67]

$$G^<(t,t') = \int du\,dv\ G^R(t,u)\Sigma^<(u,v)[G^R(t',v)]^\dagger \tag{15}$$

with $\Sigma^<(t,t') = \sum_{\bar{m}} \Sigma^<_{\bar{m}}(t,t')$ and $\Sigma^<_{\bar{m}}(t,t') = \mathbf{H}_{\bar{0}\bar{m}}(t)g^<_{\bar{m}}(t,t')\mathbf{H}_{\bar{m}\bar{0}}(t')$. Eqs. (11) and (15) form the starting point of this paper.

3.2. Equations of motion for lead self-energies

To get a complete set of equations, we need to relate the self-energies of the leads to the lead Hamiltonian matrices. While the corresponding calculation in the energy domain is well developed, self-energies as a function of time have been seldom calculated. Here we use the following equation of motion,

$$i\partial_t g^R_{\bar{m}}(t,t') - H_{\bar{m}}(t)g^R_{\bar{m}}(t,t') = \int du\ V_{\bar{m}}(t)g^R_{\bar{m}}(t,u)V^\dagger_{\bar{m}}(u)g^R_{\bar{m}}(u,t'). \tag{16}$$

This equation only provides the *surface* Green's function of the lead, i.e. Green's function matrix elements for the last layer of the semi-infinite periodic structure. For time-independent leads (the case studied in this paper after the gauge

transformation), $g^R_{\bar{m}}(t-t')$ is a function of the time difference $t-t'$ only. It is related by a simple Fourier transform to the surface Green's function in energy:

$$g^R_{\bar{m}}(t-t') = \int \frac{dE}{2\pi} e^{-iE(t-t')} g^R_{\bar{m}}(E). \tag{17}$$

There are many techniques to calculate $g^R_{\bar{m}}(E)$ but the presence of a cusp at $t=t'$ in the time domain and $1/\sqrt{E}$ singularities in the energy domain (whenever a new conducting channel opens) renders a Fourier transform impractical and a direct use of Eq. (16) much more convenient. The analogue of Eq. (16) in the energy domain is a self-consistent equation for $g^R_{\bar{m}}(E)$

$$g^R_{\bar{m}}(E) = 1/[E - H_{\bar{m}} - V_{\bar{m}} g^R_{\bar{m}}(E) V^\dagger_{\bar{m}}] \tag{18}$$

which is far less interesting than its time-dependent counterpart. Indeed, the corresponding iterative solution converges poorly (each iteration corresponds to adding one layer to the lead while other schemes allow to double its size at each iteration) and it requires the use of a small imaginary part in the self-energy.

As each lead is at thermal equilibrium, the Lesser surface Green's function for the lead is obtained from the Retarded one through the use of the fluctuation–dissipation theorem [68,67]:

$$g^<_{\bar{m}}(E) = -f_{\bar{m}}(E)\left(g^R_{\bar{m}}(E) - [g^R_{\bar{m}}(E)]^\dagger\right) \tag{19}$$

where $f_{\bar{m}}(E) = 1/[1+e^{(E-\mu_{\bar{m}})/k_B T_{\bar{m}}}]$ is the Fermi function of the lead.

4. Wave function (WF) approach

We now turn to the construction of our wave function approach. We seek to explicitly construct the wave function in terms of Green's functions, relate the physical observables to the wave function and derive the equations that this wave function satisfies. Eventually, we arrive at a closed set of equations where the original Green's function formalism has disappeared entirely. The central object of the resulting theory lies halfway between NEGF and the time-dependent scattering approach. Both Green's functions and the (time-dependent) scattering matrix can be obtained directly from the wave function.

In what follows we suppose that the voltage drop actually takes place *inside* the central region $\bar{0}$. This can be done without loss of generality; if it is not the case then we simply change our definition of the central region to include a few layers of the leads. We always include at least the first layer of each lead in our definition of the central region $\bar{0}$. This step is not necessary but somewhat simplifies the resulting expressions.

4.1. Construction of the wave function

We start with a representation of the lead Lesser self-energy in the energy domain:

$$\Sigma^<(t-t') = \sum_{\bar{m}} \int \frac{dE}{2\pi} i f_{\bar{m}}(E) e^{-iE(t-t')} \Gamma_{\bar{m}}(E) \tag{20}$$

where $\Gamma_{\bar{m}}(E) = i\mathbf{H}_{\bar{0}\bar{m}}\left(g^R_{\bar{m}}(E) - [g^R_{\bar{m}}(E)]^\dagger\right)\mathbf{H}_{\bar{m}\bar{0}}$ is the coupling matrix to the electrodes (also known as the tunneling rate matrix in the context of weak coupling). $\Gamma_{\bar{m}}(E)$ can be diagonalized into

$$\Gamma_{\bar{m}}(E) = \sum_\alpha v_{\bar{m}\alpha} \xi_{\alpha E} \xi^\dagger_{\alpha E} \tag{21}$$

where the $\xi_{\alpha E}$ are the so-called dual transverse wave functions and $v_\alpha(E)$ is the corresponding mode velocity [69]. Note that the $\xi_{\alpha E}$ are normalized but not necessarily orthogonal. They are related to the transverse incoming modes $\xi^{in}_{\alpha E}$ to be introduced in the next section by $\xi_{\alpha E} = \Gamma_{\bar{m}}\xi^{in}_{\alpha E}/v_{\bar{m}\alpha}$. Note that alternatively we could have used the fact that $\Gamma_{\bar{m}}$ is a Hermitian matrix to justify its diagonalization into a set of *orthonormal* vectors. However, by doing so we would have mixed outgoing and incoming states and lost the connection with the scattering theory described in the next section. We also note that all modes are in principle included but the evanescent ones have vanishing velocities and will therefore automatically drop out of the problem.

Eq. (15) for the Lesser Green's function, hence the observables, can be recast using the two above equations into,

$$G^<(t,t') = \sum_\alpha \int \frac{dE}{2\pi}\, i f_\alpha(E) \Psi_{\alpha E}(t) \Psi_{\alpha E}(t')^\dagger \tag{22}$$

where we have used a unique index α to denote both the leads and the channels inside the leads and introduced the wave function,

$$\Psi_{\alpha E}(t) = \sqrt{v_\alpha} \int du\, G^R(t,u) e^{-iEu} \xi_{\alpha E}. \tag{23}$$

$\Psi_{\alpha E}(t)$ is the projection inside the device region of $\psi_{\alpha E}(t)$ which is defined in the infinite system: $\Psi_{\alpha E} = [\psi_{\alpha E}]_{\bar{0}}$ with

$$\psi_{\alpha E}(t) = \sqrt{v_\alpha} \int du\, \mathcal{G}^R(t,u) e^{-iEu} \xi_{\alpha E}. \tag{24}$$

$\Psi_{\alpha E}(t)$ and $\psi_{\alpha E}(t)$ are the basic objects that will be discussed from now on.

We note that the Retarded Green's function $G^R(t,t') = \theta(t-t')[G^>(t,t') - G^<(t,t')]$ can also be obtained from the wave function,

$$G^R(t,t') = -i\theta(t-t') \int \frac{dE}{2\pi} \sum_\alpha \Psi_{\alpha,E}(t) \Psi^\dagger_{\alpha,E}(t') \tag{25}$$

from which we get the normalization condition,

$$\forall\, t \quad \int \frac{dE}{2\pi} \sum_\alpha \Psi_{\alpha,E}(t) \Psi^\dagger_{\alpha,E}(t) = \mathbb{1}_{\bar{0}}. \tag{26}$$

4.2. Effective Schrödinger equation

The equations satisfied by the wave function derive directly from the equation of motion for the Retarded Green's function. They read,

$$i\partial_t \Psi_{\alpha E}(t) = \mathbf{H}_{\bar{0}\bar{0}}(t) \Psi_{\alpha E}(t) + \int du\, \Sigma^R(t-u) \Psi_{\alpha E}(u) + \sqrt{v_\alpha} e^{-iEt} \xi_{\alpha E} \tag{27}$$

and

$$i\partial_t \psi_{\alpha E}(t) = \mathbf{H}(t) \psi_{\alpha E}(t) + \sqrt{v_\alpha} e^{-iEt} \xi_{\alpha E}. \tag{28}$$

Remarkably, Eq. (28) is almost the Schrödinger equation, up to the source term $\sqrt{v_\alpha} e^{-iEt} \xi_{\alpha E}$. Together, Eqs. (22) and (27) (or alternatively Eq. (28)) form a closed set of equations that permits the calculation of the observables of the system. In particular, the Retarded Green's function does not appear explicitly anymore. Note that the initial conditions for the wave functions are not well defined. We shall find, however, that they are essentially irrelevant and that after some relaxation time they are forgotten; the source term controls the results (see Fig. 6).

At this stage, several routes could be followed. If we suppose the time-dependent perturbations to be periodic, we can make use of the Floquet theorem to obtain a Floquet based wave function approach. Here, however, we concentrate on the physics of pulses (perturbations of any sort but localized in time). We suppose that the system is in a stationary state up to a time $t = 0$ and that the time-dependent perturbations (voltage pulses, microwaves, etc.) are switched on at time $t > 0$. We separate the problem into a stationary part and a time-dependent perturbation $\mathbf{H}_{\bar{0}\bar{0}}(t) = \mathbf{H}_{\bar{0}st} + \mathbf{H}_{\bar{0}w}(t)$. The solution of the stationary problem takes the form $e^{-iEt} \Psi^{st}_{\alpha E}$, where the stationary solution can be obtained by solving the linear (sparse) equation,

$$[E - \mathbf{H}_{\bar{0}st} - \Sigma^R(E)] \Psi^{st}_{\alpha E} = \sqrt{v_\alpha} \xi_{\alpha E} \tag{29}$$

$\Psi^{st}_{\alpha E}$ is a typical output of wave function based algorithms for DC transport [70]. We now introduce a wave function measuring the *deviation* with respect to the stationary solution,

$$\Psi_{\alpha E}(t) = \bar{\Psi}_{\alpha E}(t) + e^{-iEt} \Psi^{st}_{\alpha E}. \tag{30}$$

$\bar{\Psi}_{\alpha E}(t)$ satisfies,

$$i\partial_t \bar{\Psi}_{\alpha E}(t) = \mathbf{H}_{\bar{0}\bar{0}}(t) \bar{\Psi}_{\alpha E}(t) + \int_0^t du\, \Sigma^R(t-u) \bar{\Psi}_{\alpha E}(u) + \mathbf{H}_{\bar{0}w}(t) e^{-iEt} \Psi^{st}_{\alpha E} \tag{31}$$

with the initial condition $\bar{\Psi}_{\alpha E}(t=0) = 0$. Eq. (31) is very similar to Eq. (27) but it has the advantage that the equilibrium physics has been removed so that the memory kernel starts at $t = 0$ (instead of $t = -\infty$). Also, the source term does not take place at the system-leads interface anymore, but rather at the sites where a time-dependent perturbation is applied. A similar treatment can be done for $\psi_{\alpha E}(t)$ and we obtain

$$i\partial_t \bar{\psi}_{\alpha E}(t) = \mathbf{H}(t) \bar{\psi}_{\alpha E}(t) + \mathbf{H}_w(t) e^{-iEt} \psi^{st}_{\alpha E} \tag{32}$$

where $\psi^{st}_{\alpha E}$ satisfies $[E - \mathbf{H}_{st}] \psi^{st}_{\alpha E} = \sqrt{v_\alpha} \xi_{\alpha E}$ and $\mathbf{H}(t) = \mathbf{H}_{st} + \mathbf{H}_w(t)$. We shall find that Eq. (31) or Eq. (32) are much more well suited for numerical simulations than the original NEGF equations (see also Appendix A for a simplified discussion in one dimension).

Finally, a common case of interest involves metallic electrodes coupled to mesoscopic systems whose characteristic energy scales are much smaller than the Fermi energy of the electrodes. In this limit (known as the wide band limit), one can neglect the energy dependence of the electrode self-energy $\Sigma^R(E+\epsilon) \approx \Sigma^R(E)$ and the self-energy memory kernel becomes local in time resulting in,

$$i\partial_t \bar{\Psi}_{\alpha E}(t) = [\mathbf{H}_{\bar{0}\bar{0}}(t) + \Sigma^R(E)] \bar{\Psi}_{\alpha E}(t) + \mathbf{H}_{\bar{0}w}(t) e^{-iEt} \Psi^{st}_{\alpha E}. \tag{33}$$

5. Time-dependent scattering theory

So far our starting point has been the NEGF formalism from which we have constructed the wave function $\Psi_{\alpha E}(t)$. We now turn to a "Landauer–Buttiker" scattering approach of time-dependent quantum transport in a mixed time-energy representation. We construct the time-dependent scattering states of the system and find that their projection inside the central region is in fact the wave function $\Psi_{\alpha E}(t)$. Hence, we shall establish (as it is the case for DC transport) that the corresponding scattering approach is rigorously equivalent to the NEGF formalism. Last, we shall make the connection with the partition free approach thereby completing the formalism part of this article. Note that the proofs below are a bit technical. Appendix A illustrates them in the simplified case of a one dimensional model.

5.1. Conducting modes in the leads

We start by introducing the plane waves α inside a lead $\bar{p}$ which take the form $\xi^{in}_{\bar{p}\alpha}(E)e^{-iEt-ik^{in}_{\alpha}(E)x}$ for the incoming states and $\xi^{out}_{\bar{p}\alpha}(E)e^{-iEt+ik^{out}_{\alpha}(E)x}$ for the outgoing ones. The integer x labels the different layers of the lead ($x \in \{1, 2, 3\cdots\}$) counted from the central system. The normalized vectors $\xi^{out}_{\bar{p}\beta}$ ($\xi^{in}_{\bar{p}\beta}$) are the transverse part of the mode for the outgoing (incoming) states, including the evanescent modes (although those will eventually drop out for the incoming part). As the plane waves satisfy the Schrödinger equation, we obtain

$$[H_{\bar{p}} - E + V_{\bar{p}}\lambda_{\alpha} + V^{\dagger}_{\bar{p}}\lambda^{-1}_{\alpha}]\xi^{out}_{\bar{p}\alpha}(E) = 0 \tag{34}$$

with $\lambda_{\alpha} = e^{+ik^{out}_{\alpha}(E)}$. $\xi^{in}_{\bar{p}\alpha}(E)$ obeying the same equation with negative momenta. This (2^{nd} order) equation can be recast in the form of a generalized eigenvalue problem,

$$\begin{pmatrix} H_{\bar{p}} - E & V^{\dagger}_{\bar{p}} \\ 1 & 0 \end{pmatrix}\begin{pmatrix} \xi_{\bar{p}\alpha}(E) \\ \chi_{\bar{p}\alpha}(E) \end{pmatrix} = \lambda_{\alpha}\begin{pmatrix} -V_{\bar{p}} & 0 \\ 0 & 1 \end{pmatrix}\begin{pmatrix} \xi_{\bar{p}\alpha}(E) \\ \chi_{\bar{p}\alpha}(E) \end{pmatrix} \tag{35}$$

for which efficient techniques have now been developed [69,71] ($\chi_{\bar{p}\alpha}(E)$ is defined by the second line of Eq. (35)). We note that solving Eq. (34) can be non trivial when V is not invertible, a common case when the lattice has more than one atom per unit cell (e.g. graphene). The corresponding mode velocity is given by $v^{out}_{\bar{p}\alpha} = i(\xi^{out}_{\bar{p}\alpha})^{\dagger}[Ve^{+ik^{out}_{\alpha}(E)} - V^{\dagger}e^{-ik^{out}_{\alpha}(E)}]\xi^{out}_{\bar{p}\alpha}$. An interesting relation is obtained by observing that $\xi^{out}_{\bar{p}\alpha}(E)$ ($\xi^{in}_{\bar{p}\alpha}(E)$) are the eigenvectors of the Retarded (Advanced) Green's function of the lead,

$$g^{R}_{\bar{p}}(E)V^{\dagger}_{\bar{p}}\xi^{out}_{\bar{p}\alpha}(E) = e^{+ik^{out}_{\alpha}(E)}\xi^{out}_{\bar{p}\alpha}(E) \tag{36}$$

$$[g^{R}_{\bar{p}}(E)]^{\dagger}V^{\dagger}_{\bar{p}}\xi^{in}_{\bar{p}\alpha}(E) = e^{-ik^{in}_{\alpha}(E)}\xi^{in}_{\bar{p}\alpha}(E) \tag{37}$$

as can be shown using Eqs. (18) and (34), see Ref. [69]. Eq. (34) implies that for any two modes (incoming or outgoing) [69],

$$(\lambda_{\alpha} - [\lambda^{*}_{\beta}]^{-1})\xi^{in/out}_{\bar{p}\beta}(E)[V_{\bar{p}}\lambda_{\alpha} - V^{\dagger}_{\bar{p}}\lambda^{*}_{\beta}]\xi^{in/out}_{\bar{p}\alpha}(E) = 0. \tag{38}$$

It follows that, while in general different modes are not orthogonal, they satisfy

$$[\xi^{out}_{\bar{p}\alpha}(E)]^{\dagger}\Gamma_{\bar{p}}\xi^{out}_{\bar{m}\beta}(E) = \delta_{\alpha\beta}\delta_{\bar{m}\bar{p}}v^{out}_{\bar{p}\alpha} \tag{39}$$

with a similar expression for the incoming modes.

5.2. Construction of the scattering states

Our aim is to construct a wave function $\psi^{scat}_{\alpha E}(t)$ which (i) is a solution of the Schrödinger equation and (ii) corresponds to an incoming plane wave in mode α (belonging to lead $\bar{m}$) with energy E. This boundary condition amounts to imposing the *incoming* part of the wave function, and leaving the outgoing part free. In particular, the system being time-dependent, the outgoing part can contain many different energies. In the rest of this section, we often drop the indices E and α when there is no risk of confusion. The value of $\psi^{scat}_{\alpha E}(t)$ are noted $\psi^{scat}_{\bar{0}}(t)$ in the central region and $\psi^{scat}_{\bar{p}x}(t)$ in the xth layer of lead $\bar{p}$. In the leads, the wave function is formed by a superposition of plane waves,

$$\psi^{scat}_{\bar{p}x}(t) \equiv \psi^{in}_{\bar{p}x}(t) + \psi^{out}_{\bar{p}x}(t) \text{ with} \tag{40}$$

$$\psi^{in}_{\bar{p}x}(t) = \delta_{\bar{p}\bar{m}}\frac{\xi^{in}_{\bar{p}\alpha}(E)}{\sqrt{|v^{in}_{\bar{m}\alpha}|}}e^{-iEt-ik^{in}_{\alpha}(E)x}$$

$$\psi^{out}_{\bar{p}x}(t) = \int\frac{dE'}{2\pi}\sum_{\beta}\frac{\xi^{out}_{\bar{p}\beta}(E')}{\sqrt{|v^{out}_{\bar{p}\beta}|}}e^{-iE't+ik^{out}_{\beta}(E')x}S_{\bar{p}\beta,\bar{m}\alpha}(E', E).$$

$S_{\bar{p}\beta,\bar{m}\alpha}(E',E)$ is the central object of the scattering theory, namely the probability amplitude for a mode α with energy E to be transmitted ($\bar{p}\neq\bar{m}$) or reflected ($\bar{p}=\bar{m}$) into mode β with energy E'. The formalism only differs from its time-independent counterpart by the possibility to absorb or emit energy. The normalization has been chosen so that the waves carry a current (per energy unit) unity. As Eq. (40) is made of a superposition of the eigenstates of the leads, it satisfies the time-dependent Schrödinger equation in the lead by construction. Eq. (40) forms an "incoming" boundary condition. One proceeds by writing the Schrödinger equation in the central region and in the first layer of the leads (the "matching conditions"):

$$i\partial_t\psi^{scat}_{\bar{0}}(t)=\mathbf{H}_{\bar{0}\bar{0}}\psi^{scat}_{\bar{0}}(t)+\sum_{\bar{p}}V_{\bar{p}}\psi^{scat}_{\bar{p}1}(t) \tag{41}$$

$$i\partial_t\psi^{scat}_{\bar{p}1}=H_{\bar{p}}\psi^{scat}_{\bar{p}1}(t)+V^{\dagger}_{\bar{p}}P_{\bar{p}}\psi^{scat}_{\bar{0}}(t)+V_{\bar{p}}\psi^{scat}_{\bar{p}2}(t), \tag{42}$$

where the projector $P_{\bar{p}}$ projects the wave function of the central region on the sites which are attached to the reservoir $\bar{p}$. The set of the three above equations fully defines the scattering states as well as the "scattering matrix" $S_{\bar{p}\beta,\bar{m}\alpha}$ of the system.

5.3. Connection to the wave function approach

To proceed, we note that as $\psi^{scat}_{\bar{p}x}(t)$ satisfies $i\partial_t\psi^{scat}_{\bar{p}1}=H_{\bar{p}}\psi^{scat}_{\bar{p}1}(t)+V^{\dagger}_{\bar{p}}\psi^{scat}_{\bar{p}0}(t)+V_{\bar{p}}\psi^{scat}_{\bar{p}2}(t)$, Eq. (42) results in,

$$V^{\dagger}_{\bar{p}}P_{\bar{p}}\psi^{scat}_{\bar{0}}(t)=V^{\dagger}_{\bar{p}}\psi^{scat}_{\bar{p}0}(t) \tag{43}$$

which relates the scattering matrix on the right to the wave function inside the system on the left.

We now use the fact that $\xi^{out}_{\bar{p}\alpha}(E)$ and $\xi^{in}_{\bar{p}\alpha}(E)$ are the eigenvectors of the Retarded and Advanced surface Green's function of the lead $\bar{p}$. Eqs. (36), (37) and (40) provide,

$$V_{\bar{p}}\psi^{out}_{\bar{p}1}(t)=\int du\,\Sigma^{R}_{\bar{p}}(t-u)\psi^{out}_{\bar{p}0}(u). \tag{44}$$

Finally, inserting the explicit decomposition Eq. (40) in terms of incoming and outgoing waves inside Eq. (41) and using Eqs. (43) and (44), we obtain,

$$i\partial_t\psi^{scat}_{\bar{0}}(t)=\mathbf{H}_{\bar{0}\bar{0}}\psi^{scat}_{\bar{0}}(t)+\sum_{\bar{p}}\int_{-\infty}^{t}du\,\Sigma^{R}_{\bar{p}}(t-u)P_{\bar{p}}\psi^{scat}_{\bar{0}}(u)+i\Gamma_{\bar{m}}(E)\psi^{in}_{\bar{m}0}(t). \tag{45}$$

Eq. (45) is identical to our main wave Eq. (27) which completes the proof that

$$\psi^{scat}_{\bar{0}}(t)=\Psi_{\alpha E}(t). \tag{46}$$

Hence the equivalence between the scattering approach and the NEGF formalism can be extended to time-dependent transport. We note however that $\psi_{\alpha E}(t)$ and the Scattering state $\psi^{scat}_{\alpha E}(t)$ do not match outside of the scattering region as the former only contains outgoing modes (and no incoming ones).

5.4. Generalization of the Fisher–Lee formula

Besides proving the formal equivalence between the Scattering and NEGF approaches in this context, the above construction provides an explicit link between the wave function and the scattering matrix. Indeed, using the definition Eq. (40) of the scattering matrix, one obtains after integration over time,

$$S_{\bar{p}\beta,\bar{m}\alpha}(E',E)=\int dt'\,e^{iE't'}\frac{[\xi^{out}_{\bar{p}\beta}(E')]^{\dagger}}{\sqrt{|v^{out}_{\bar{m}\alpha}(E')|}}\Gamma_{\bar{p}}(E')[\psi^{scat}_{\bar{p}0,\alpha E}(t')-\psi^{in}_{\bar{p}0,\alpha E}(t')]. \tag{47}$$

Eq. (47) is a generalization of the Fisher–Lee relation [72] for time-dependent problems. As the numerical algorithms described in the later sections allow one to compute the wave function $\psi^{scat}_{\bar{p}0,\alpha E}(t')$ directly, they also provide means to evaluate the scattering matrix through the above relation. Eq. (47) can be further simplified into,

$$S_{\bar{p}\beta,\bar{m}\alpha}(E',E)=\frac{[\xi^{out}_{\bar{p}\beta}(E')]^{\dagger}}{\sqrt{|v^{out}_{\bar{m}\alpha}(E')|}}\Gamma_{\bar{p}}(E')\left[\int dt'\,e^{iE't'}\psi^{scat}_{\bar{p}0,\alpha E}(t')-\frac{\xi^{in}_{\bar{m}\alpha}(E')}{\sqrt{|v^{in}_{\bar{m}\alpha}(E)|}}2\pi\delta(E'-E)\right]. \tag{48}$$

Inserting the definition of the wave function in terms of the Retarded Green's function inside Eq. (48), one obtains another form, closer to the original one of Ref. [72],

$$S_{\bar{p}\beta,\bar{m}\alpha}(E',E)=\frac{[\xi^{out}_{\bar{p}\beta}(E')]^{\dagger}}{\sqrt{|v^{out}_{\bar{m}\alpha}(E')|}}\Gamma_{\bar{p}}(E')\left[\mathcal{G}^{R}(E',E)\Gamma_{\bar{m}}(E)-2\pi\delta(E'-E)\delta_{\bar{m}\bar{p}}\right]\frac{\xi^{in}_{\bar{m}\alpha}(E)}{\sqrt{|v^{in}_{\bar{m}\alpha}(E)|}} \tag{49}$$

where we have introduced the (double) Fourier transform of the Retarded Green's function,

$$\mathcal{G}^R(E', E) = \int dt dt' \, \mathcal{G}^R(t', t) e^{iE't' - iEt}. \tag{50}$$

5.5. Link with the partition-free initial condition approach

In the construction of the scattering states given above, we impose a boundary condition where the form of the incoming modes is fixed *for all times* while the outgoing modes are free. Hence, this construction treats incoming modes and outgoing ones on different footings. This might seem correct based on physical arguments, yet we have seen in Section 4 that the matrix Γ could be diagonalized in several different ways. In the rest of this section, we follow a very simple route taken by Cini [3] and further developed in Refs. [4,64,65,73] where such a distinction does not appear explicitly. The approach is conceptually very simple. Let us suppose that the Hamiltonian is time-independent up to $t = 0$, then for $t < 0$ we assume that the system is in an incoherent superposition of all the eigenstates $e^{-iEt}\psi^{st}_{\alpha E}$ of the system with a filling factor $f_\alpha(E)$ (this may be thermal equilibrium as in Ref. [64] or more generally a non-equilibrium stationary state). At time $t > 0$ the corresponding states $\psi^{init}_{\alpha E}(t)$ simply evolve according to the Schrödinger equation $i\partial_t \psi^{init}_{\alpha E}(t) = \mathbf{H}(t)\psi^{init}_{\alpha E}(t)$ with the initial condition $\psi^{init}_{\alpha E}(t = 0) = \psi^{st}_{\alpha E}$. Apparently, this is a different boundary condition from the one of the scattering state above.

We now use the block structure of the Schrödinger equation (projected on lead $\bar{p}$) and obtain after integration between 0 and t (momentarily dropping the indices E and α),

$$\psi^{init}_{\bar{p}}(t) + i g^R_{\bar{p}}(t)\psi^{init}_{\bar{p}}(0) = \int_0^t du g^R_{\bar{p}}(t-u)\mathbf{H}_{\bar{p}\bar{0}}\psi^{init}_{\bar{0}}(u) \tag{51}$$

from which we get (after substitution inside the equation for $\psi^{init}_{\bar{0}}$),

$$i\partial_t \psi^{init}_{\bar{0}}(t) = \mathbf{H}_{\bar{0}\bar{0}}(t)\psi^{init}_{\bar{0}}(t) + \int_0^t du \Sigma^R(t-u)\psi^{init}_{\bar{0}}(u) - i\sum_{\bar{p}} \mathbf{H}_{\bar{0}\bar{p}} g^R_{\bar{p}}(t)\psi^{init}_{\bar{p}}(0). \tag{52}$$

Eq. (52) is essentially Eq. (4) of Ref. [4]. Eq. (52) is very similar to Eq. (31) with a crucial practical difference: in the latter, the source term is present only at the system's sites which are time-dependent while in the former it takes place at the system-lead interfaces. Introducing $\bar{\psi}^{init}_{\alpha E}(t) \equiv \psi^{init}_{\alpha E}(t) - e^{-iEt}\psi^{st}_{\alpha E}$, we find that $\bar{\psi}^{init}_{\bar{0}}(t)$ obeys Eq. (31) with $\bar{\psi}^{init}_{\bar{0}}(t = 0) = 0$. Hence, we have proved one more equivalence, between the wave function $\bar{\Psi}_{\alpha E}(t)$ and $\bar{\psi}^{init}_{\bar{0}}(t)$:

$$\psi^{init}_{\alpha E\bar{0}}(t) = \Psi_{\alpha E}(t). \tag{53}$$

We note that the equivalence requires that the initial states at $t = 0$ are the scattering states $\psi^{st}_{\alpha E}$ of the stationary system. When the system contains more than one channel, one finds that any choice of the initial condition $\sum_\alpha U_{a\alpha}\psi^{st}_{\alpha E}$, where U is a unitary matrix, eventually gives the same total current and is therefore also equivalent to the NEGF theory. However, the matrix U must be unitary which fixes the normalization of the initial states; they must carry a current unity.

5.6. "Floquet wave function" and link with the Floquet scattering theory

Although this paper focuses on time-resolved electronics (typically transient regimes or voltage pulses), the wave function formalism can also be used for perturbations periodic in time. We refer to [22] for an introduction and bibliography on the subject. Let us briefly consider the situation where $\mathbf{H}_{\bar{0}\bar{0}}(t + T) = \mathbf{H}_{\bar{0}\bar{0}}(t)$ and introduce its decomposition in terms of harmonics of $\omega = 2\pi/T$,

$$\mathbf{H}_{\bar{0}\bar{0}}(t) = \sum_{n=-\infty}^{\infty} H_n e^{-in\omega t}. \tag{54}$$

We also define the Fourier transform $\Psi_{\alpha E}(E')$ of $\Psi_{\alpha E}(t)$,

$$\Psi_{\alpha E}(E') = \int dt' \, e^{iE't'}\Psi_{\alpha E}(t') \tag{55}$$

from which we can express Eq. (27) as,

$$E'\Psi_{\alpha E}(E') = \sum_n H_n \Psi_{\alpha E}(E' - n\omega) + \Sigma^R(E')\Psi_{\alpha E}(E') + 2\pi\delta(E' - E)\sqrt{v_\alpha}\xi_{\alpha E}. \tag{56}$$

Introducing $\epsilon \in [-\omega/2, \omega/2]$ and m such that $E' = E + \epsilon + m\omega$, one defines $\Psi_m(\epsilon) \equiv \Psi_{\alpha E}(E + \epsilon + m\omega)$ which verifies,

$$\epsilon\Psi_m(\epsilon) = \sum_n H_n \Psi_{m-n}(\epsilon) + [\Sigma^R(E + \epsilon + m\omega) - m\omega - E]\Psi_m(\epsilon) + 2\pi\delta(\epsilon)\delta_{m,0}\sqrt{v_\alpha}\xi_{\alpha E}. \tag{57}$$

Last, we define

$$\psi_{\alpha E\epsilon}(t) = \sum_m e^{-im\omega t}\Psi_m(\epsilon) \tag{58}$$

and obtain

$$\Psi_{\alpha E}(t) = \int_{-\omega/2}^{\omega/2} \frac{d\epsilon}{2\pi} e^{-iEt - i\epsilon t}\psi_{\alpha E\epsilon}(t) \tag{59}$$

$\psi_{\alpha E\epsilon}(t)$ verifies $\psi_{\alpha E\epsilon}(t+T) = \psi_{\alpha E\epsilon}(t)$ so that Eq. (59) corresponds in fact to Floquet theorem. We also note that the source term in Eq. (57) is only present at $\epsilon = 0$ so that the other energies do not contribute to the scattering wave function. Taking this last point into account and computing (as an example) the current $I_{ij}(t)$ between site i and site j, we arrive at,

$$I_{ij}(t) = -2\,\mathrm{Im}\sum_\alpha \int \frac{dE}{2\pi} f_\alpha(E) \sum_{n,m,p} \Psi^*_{\alpha E,m}(i)[H_n]_{ij}\Psi_{\alpha E,p}(j)e^{-i(n-m+p)\omega t} \tag{60}$$

where the wave function $\Psi_{\alpha E,n}(i)$ at site i satisfies,

$$[E + m\omega - \Sigma^R(E+m\omega)]\Psi_{\alpha E,m} - \sum_n H_n\Psi_{\alpha E,m-n} = \delta_{m,0}\sqrt{v_\alpha}\xi_{\alpha E}. \tag{61}$$

Eqs. (60) and (61) provide a complete set of equations to compute the current of the system. The corresponding "Floquet wave function" can be put in direct relation to Floquet Scattering theory using the link with the Scattering matrix established at the beginning of this section. In practice, the infinite set of equations defined by Eq. (61) needs to be truncated somehow [25] and one is left with solving a large, yet finite, system of linear equations. Alternatively, a systematic perturbation theory can be constructed taking the AC Hamiltonian as a small perturbation [23].

We have thus made explicit connections between various theoretical frameworks: the NEGF, the scattering approach, the partition-free initial condition approach and, for perturbations that are periodic in time, the scattering Floquet approach. This concludes the formalism part of this paper. We now turn to a discussion of the strategies that can be implemented to perform numerical simulations of the corresponding theories. The formalism is also suitable for analytical approaches, and some results will be given toward the end of this paper.

6. Strategies for efficient numerical simulations

We now turn to a discussion of various algorithms for simulating the formalism introduced above. Here we provide a concrete example of an application to a simple one dimensional chain, but the algorithms are general and apply to arbitrary dimensions and geometries. In fact, we aim at developing a general algorithm that would allow one to tackle a rather large class of problems, in the same spirit as the existing numerical toolkits for the transport properties of stationary devices [74,70]. Our Hamiltonian reads,

$$\hat{\mathbf{H}}(t) = -\gamma \sum_{i=-\infty}^{+\infty} c^\dagger_{i+1}c_i - \gamma[e^{i\phi(t)} - 1]c^\dagger_2 c_1 + \sum_{i=1}^{N}\epsilon_i c^\dagger_i c_i + h.c. \tag{62}$$

where the system is subjected to a voltage pulse $w(t)$ with $\phi(t) = \int_{-\infty}^t du\ w(u)$ and ϵ_i the potential inside the central region $\bar{0} = \{1, 2, \ldots, N\}$. The ϵ_i can in principle be time-dependent but we restrict the examples to static cases; all the time dependence comes from the voltage drop between site 1 and site 2. During the development of the numerical techniques presented below, we used various analytical results to perform consistency checks of the validity of the numerics. They are summarized in Appendix C.

We denote N the total number of sites of the central region and S the number of sites connected to the electrodes (for a cubic system in d dimensions we have $N \sim L^d$ and $S \sim L^{d-1}$). Let us call $t_{\max}$ the maximum time of the simulations and h_t the typical discretization time step. In this section, we introduce the various algorithms (three for NEGF labeled GF-A,B and C as well as four for the wave function approach labeled WF-A, B, C and D) before turning to the numerics in the next section. We emphasize that, although these algorithms have very different computing efficiencies, they are all mathematically equivalent and – as we have checked explicitly – give the same numerical results.

6.1. GF-A: brute-force integration of the NEGF equations

The first technique consists in directly integrating the equations of motion of the NEGF formalism treating the integro-differential equations as ordinary differential equations. However, the right hand sides of the equations contain the self-energy integrals that need to be re-evaluated every time step. This also means that some values of the Retarded Green's function in the past must be kept in memory. The algorithm consists of 3 steps. (i) One starts with a calculation of the leads' self-energy by a direct integration of Eq. (16) for the $S \times S$ surface Green's function of the leads. (ii) In the second step, one

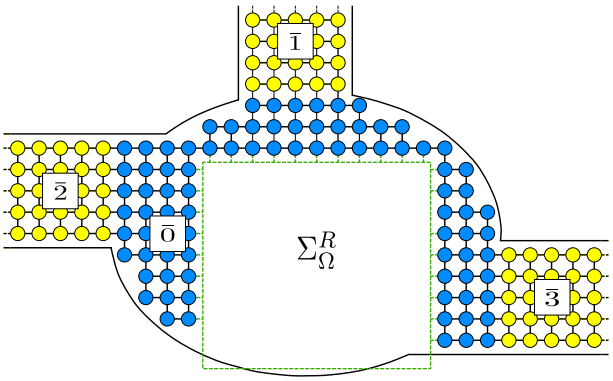

Fig. 2. Sketch of the GF-B scheme. The degrees of freedom of the region Ω inside the dashed green square are integrated out in a self-energy term denoted by Σ^R_Ω. This integration leads to an effective system containing a reduced number of sites. (For interpretation of the references to color in this figure legend, the reader is referred to the web version of this article.)

proceeds and integrates Eq. (11) which has a rather similar structure. (iii) The last step is the calculation of the Lesser Green's function using the double integration of Eq. (15). This last step is quite problematic as the integration over times takes place over an infinite time window (as opposed to the calculation of the Retarded Green's function where the self-energy terms only span a finite window due to the causality of the Retarded Green's function). In practice, one has to resort to using a cutoff within a large time window Δ_t. We can already note that the CPU cost of all these three steps scale as the square of the total time, either $(t_{\max}/h_t)^2$ or $(\Delta_t/h_t)^2$ and that the calculations of various observables (for different times for instance) involve separate calculations for the last step. For implementation purposes, we note that the integrals containing the self-energy terms can be parallelized by dividing the integral range into smaller pieces, which can be used to speed up the calculations. For integrating the equations of motion, we use either an implicit linear multi-step scheme [75] or an explicit 3rd order Adams–Bashforth scheme (with slightly better performances for the latter). Overall, the GF-A approach quickly becomes prohibitively expensive in CPU time. This may explain why (to the best of our knowledge) the simulations performed so far within this approach have been restricted to very small systems and times.

6.2. GF-B: Integrating out the time-independent subparts of the device

A first strategy to improve on the direct (naive) GF-A approach described above is to integrate out the parts of the device region where we do not want to compute observables. A typical example is shown in Fig. 2. Suppose that a subset Ω of the sites in region $\bar{0}$ has a "sub" Hamiltonian matrix $\mathbf{H}_\Omega(t)$. The Green's function for the *isolated* region Ω (i.e. when the coupling to the rest of region $\bar{0}$ is zero) can be obtained by simply integrating the equation of motion of the finite region $i\partial_t g^R_\Omega(t,t') = \mathbf{H}_\Omega(t) g^R_\Omega(t,t')$. This is particularly simple when the region Ω is time-independent: diagonalizing the finite matrix $\mathbf{H}_\Omega \chi_\alpha = \epsilon_\alpha \chi_\alpha$, the Retarded Green's function simply reads,

$$g^R_\Omega(t-t') = -i\theta(t-t') \sum_\alpha e^{-i\epsilon_\alpha (t-t')} \chi_\alpha \chi^\dagger_\alpha. \tag{63}$$

Note that Eq. (63) contrasts with its counterpart in the energy domain: the Retarded Green's function as a function of energy of a finite region is very ill defined numerically as it is essentially a sum of Dirac distributions. Noting $\mathbf{H}_{\bar{0}\Omega}$ the matrix elements coupling the Ω region to the rest of the device region $\bar{0}$, we introduce the self-energy due to the Ω region,

$$\Sigma^R_\Omega(t,t') = \mathbf{H}_{\bar{0}\Omega}(t) g^R_\Omega(t,t') \mathbf{H}_{\Omega\bar{0}}(t'). \tag{64}$$

We can now proceed with solving Eq. (11) for the smaller region $\bar{0} \setminus \Omega$ with the added Σ^R_Ω in the self-energy,

$$\Sigma^R(t,t') \to \Sigma^R(t,t') + \Sigma^R_\Omega(t,t'). \tag{65}$$

Note however that the Lesser self-energy is *unchanged* as the Ω region is not a lead (i.e. is not at thermal equilibrium). Using this procedure, any region can be integrated out of the device region, effectively reducing the effective total size N of the simulation, but at the cost of increasing the number of surface sites S.

When the size of the Ω region becomes large, a direct calculation of $\Sigma^R_\Omega(t,t')$ becomes impractical. Fortunately, many schemes that have been developed in the energy domain can be transposed to the time domain: the original recursive Green's function algorithm, its variant the knitting algorithm [74] or the more involved nested dissection algorithm [76,77]. These schemes can be discussed using the self-energy introduced above to "decimate" parts of the system, but they are perhaps more transparent when discussed in the context of the Dyson equation. Let $H_{ab}(t)$ be the Hamiltonian matrix of a system and let one decompose it into the sum of two terms $H_{ab} = H_a + H_b$ (typically H_a will be the Hamiltonian matrix for

two disconnected regions and H_b connects these two regions together) and we note G^R_{ab} (G^R_a) the Retarded Green's function associated with H_{ab} (H_a). In this context, the Dyson equation reads,

$$G^R_{ab}(t,t') = G^R_a(t,t') + \int du\, G^R_a(t,u) H_b(u) G^R_{ab}(u,t'). \tag{66}$$

Eq. (66) allows the separated parts of the systems to be merged (note that the structure in time of this equation is "triangular", i.e. one can solve it for t close to t' and iteratively increase t). We refer to Ref. [74] for a detailed discussion of the procedure used for glueing isolated parts together. Applying Eq. (66) recursively in a (quasi) one dimensional geometry, one can add one slice of the system at each iteration until the full system has been added (Recursive Green's function algorithm). Adding the sites one at a time, one obtains the knitting algorithm which allows one to handle systems of arbitrary geometries. Both algorithms have CPU times that scale as $S^2N(\Delta_t/h_t)^2$ but memory footprints much smaller than the direct method. In the last algorithm, nested dissection, one cuts the system recursively into 2 (or more) pieces until the pieces are small enough that their individual Green's functions may be calculated directly. The gluing sequence is then applied backward to reconstruct the Retarded Green's function of the full system. Note that the nested dissection algorithm suffers from stability problems in the energy domain as some of the pieces are not in contact with the leads (and thus suffers from the problem discussed in the beginning of this subsection). In the time domain, however, no such limitation occurs.

6.3. GF-C: integration scheme that preserves unitarity

In GF-A and GF-B, we use simple discretization schemes to integrate the integro-differential equations for the Retarded Green's functions. However, these schemes (as well as others, such as the Runge–Kutta method) do not enforce unitarity of the evolution operator in Eq. (9). The scheme GF-C builds on GF-B but one replaces the discretization scheme by one that preserves this important property of quantum propagation.

Eq. (9) implies that for any intermediate time $u \in [t', t]$ we have,

$$\mathcal{G}^R(t,t') = i\mathcal{G}^R(t,u)\mathcal{G}^R(u,t'). \tag{67}$$

which has a simple interpretation in terms of path integral: the propagator between t' and t is a sum over all possible paths and this formula reflects the fact that we keep track of the site where the particle is at time u. As the particle may be in the central region or in one of the leads at time u we get, after integrating over the degrees of freedom of the leads (see Appendix B for the derivation),

$$G^R(t,t') = iG^R(t,u)G^R(u,t') + \int_u^t dv \int_{t'}^u dv'\, G^R(t,v)\Sigma^R(v,v')G^R(v',t'). \tag{68}$$

Eq. (68) is a sum of two terms which depend on the position of the particle at time u. The first term corresponds to a particle which is in the central region at time u while the second term accounts for the paths entering the leads at $v' < u$ and returning to the central region at a later time $v > u$ (i.e. the particle is in the lead at time u). Eq. (68) encapsulates the unitarity of the evolution operator by construction. It can be used to realize an efficient explicit integration scheme for the Retarded Green's function. Applying Eq. (68) with $t \to t + h_t$ and $u \to t$ we obtain:

$$G^R(t+h_t,t') = iA_{h_t}(t)G^R(t,t') + \frac{h_t}{2}\int_{t'}^t dv[A_{h_t}(t)\Sigma^R(t,v) - i\Sigma^R(t+h_t,v)]G^R(v,t') \tag{69}$$

where $A_{h_t}(t)$ is the short time propagator $A_{h_t}(t) = G^R(t+h_t,t)$. Eq. (69) provides an explicit scheme for integrating the equation of motion which proves to be more stable than the naive ones. Note that the Hamiltonian matrix has disappeared from Eq. (69). It is hidden in the short time propagator, $A_{h_t}(t)$, which can be obtained "exactly" from a direct integration of the equation of motion Eq. (11) using a very small time step (much smaller than h_t). The computing time to get this very precise estimate is $\propto h_t^2$ and, h_t being small, therefore negligible.

6.4. WF-A: direct integration of Eq. (27)

We now turn to the algorithms based on the wave function approach. We shall see that they are much simpler and efficient than their NEGF counterparts. In the first one, WF-A, we integrate directly Eq. (27) using a 3rd order Adams–Bashforth scheme. The algorithm is intrinsically parallel as the calculations for different energies are totally independent. In a second step, we calculate the energy integral of Eq. (22) to obtain the various observables. Note that this calculation can be done *on fly* so that observables for all intermediate values of $t \leq t_{\max}$ can be obtained in a single run (in contrast to the GFs algorithms). A second level of parallelism can be introduced with the calculation of the self-energy "memory" terms. Note that in principle, the strategies developed for GF-B and GF-C could be also used for the wave function approach. We shall take a somewhat different route however. A direct advantage of the WF approaches is that the equations involved are on vectors rather than on matrices. Sophisticated optimizations could be used in order *not* to calculate all the matrix elements in the GF approaches (but only the relevant ones). However in the WF approach, one naturally calculates the minimum information needed to recover the observables.

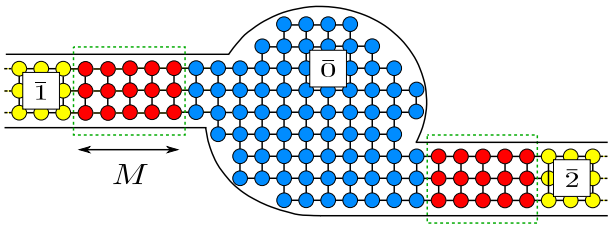

Fig. 3. Sketch of the WF-C and WF-D schemes: M layers of the leads (red) are added the central part $\bar{0}$ (blue circles) to constitute the effective central region. In WF-C the rest of the leads (yellow circles) are simply ignored while in WF-D, they are treated within the wide band approximation. (For interpretation of the references to color in this figure legend, the reader is referred to the web version of this article.)

6.5. WF-B: subtracting the stationary solution, integration of Eq. (31)

WF-B is very similar to WF-A except that we now use Eq. (31) and therefore study the *deviation* from the stationary case. Being able to "subtract" the stationary physics from the equations brings three distinct advantages compared to WF-A: (i) self-energy "memory" integrals start from $t = 0$ (instead of $t = -\infty$) removing the need for the large time cutoff Δ_t introduced earlier. In addition, the initial condition is very well defined as the wave function vanishes. (ii) for most practical physical systems, the characteristic energies involved are small compared to the Fermi energy. Subtracting the stationary physics allows one to take advantage of these features to narrow down the integration of Eq. (22) to a region close to the Fermi energy. (iii) The source terms in Eq. (31) are present only at the sites where time-dependent perturbations are present.

6.6. WF-C: from integro-differential to differential equation

The scheme WF-B is already quite efficient and renders rather large problems ($N \sim 1000$) for rather long times ($t \sim 1000\gamma^{-1}$) tractable in a reasonable CPU time (say, 1 h). Let us analyze its total CPU cost. We find, $CPU(WF - B) \propto (t/h_t)[N + S^2(t/h_t)]N_E$ where the first term comes from the (sparse) matrix vector multiplication with the Hamiltonian matrix and the second term accounts for the "memory" integral with the self-energy. The factor N_E accounts for the different energies and modes for which Eq. (32) must be integrated. In general this N_E is not an issue as all these calculations can be done in parallel and for relevant regimes the integral gets concentrated on a region close to the Fermi energy. The memory footprint is $MEM(WF - B) \propto [N + S(t/h_t)]$ as we need to keep in memory the wave function at time t in the system plus its history on the lead-system interfaces. The bottleneck of the calculation clearly comes from the "memory integral" which itself comes from the information corresponding to the wave function outside of the central region. The computational time is essentially the same as if one had studied the time evolution of a finite isolated system of $N + S^2(t/h_t)$ sites. For the typical values used here, $t = 1000\gamma^{-1}$ and $h_t = 0.01$, we find that WF-B's CPU is the same as if one was studying a finite system (i.e. no leads) of size $N = 100000$. On the other hand we know that signal propagation in the Schrodinger equation takes place at most at a speed $v = \partial E/\partial k$ with $E(k) = -2\gamma \cos k$ for a 1d chain. Hence at most $M \approx \gamma t$ layers of the lead can be probed by the propagation of the wave-function. For $t = 1000\gamma^{-1}$ this means at most 1000 layers.

The scheme WB-C is therefore very simple: instead of integrating the integro-differential Eq. (31), one integrates the much simpler differential Eq. (32). As this cannot be done for an infinite system, one simply truncates the system keeping the central region plus M layers of each leads (see Fig. 3). The expected correct value for M is $M \approx v_{mx}t/2$ with the maximum speed being $v_{mx} = \gamma \max_k |\partial E/\partial k| = \gamma z$. z is the coordinance of the system (number of neighbors per site) and the factor $1/2$ comes from the fact that the signal has to travel up to the effective boundary (yellow–red interface on Fig. 3) *and* come back in order to disturb the central region. Lower values of M can be used if the Fermi energy is close to the band edges and the system is therefore slower. According to the above analysis, only $M \sim 1000 \ll 100000$ layers should be necessary, which should lead to an important speed up compared to WF-B. It also considerably simplifies the implementation and allows for very aggressive optimizations. The expected gain is not a simple prefactor as $CPU(WF - C) \propto (t/h_t)[N + S\gamma t]N_E$ is parametrically smaller than WB-B for 2D and 3D systems.

6.7. WF-D: faster convergence using the wide band limit

The drawback of WF-C is that hardwall boundary conditions are employed at the yellow–red interface (see Fig. 3). If one does not take a large enough value of M, the particles will eventually bounce back toward the central region. WF-D is a simple generalization of WF-C where the remaining part of the leads (yellow sites in Fig. 3) are treated within the wide band limit Eq. (33) so that we effectively have "absorbing" boundary conditions and faster convergence properties with respect to M. Note that WF-D is an *exact* scheme, the (wide band limit) self-energy term is only used to accelerate the convergence with respect to M (as we shall see later in Fig. 7).

We shall see that WF-D will be by far the fastest of all the methods described in this article. We gather below the various steps associated with its practical implementation (the equations that follow were given before and are repeated here for convenience).

1. One starts with defining the Hamiltonian of the model, i.e. the two matrices $H_{\tilde{m}}$ and $V_{\tilde{m}}$ that define the Hamiltonian of each lead as well as the time-independent matrix $\mathbf{H}_{\tilde{0}st}$ for the central part and the time-dependent counterpart $\mathbf{H}_{\tilde{0}w}(t)$. In many cases (for instance for the voltage pulses discussed next), the time-dependent part of the Hamiltonian only connects a few subparts of the central region.
2. (a) One constructs the stationary modes of the leads, solving Eq. (35). (There is a large literature on this topic which we refer to, see Ref. [74] and references therein.)
   (b) One also computes the self-energy of the leads, defined by $\Sigma^R(E) = \sum_{\tilde{m}} V_{\tilde{m}} g^R_{\tilde{m}}(E) V^\dagger_{\tilde{m}}$ and Eq. (18).
3. Once the leads properties are known, one computes the stationary wave function of the system solving the following linear set of equations
$$[E - \mathbf{H}_{\tilde{0}st} - \Sigma^R(E)]\Psi^{st}_{\alpha E} = \sqrt{v_\alpha}\xi_{\alpha E}.$$
Note that steps (2a), (2b) and (3) are standard steps of quantum transport calculations in wave function based algorithms.
4. M layers of the leads are now concatenated to the central region Hamiltonian matrix $\mathbf{H}_{\tilde{0}st}$. Everything is now ready to form the main Eq. (33) of the method
$$i\partial_t \bar{\Psi}_{\alpha E}(t) = [\mathbf{H}_{\tilde{0}st} + \mathbf{H}_{\tilde{0}w}(t) + \Sigma^R(E)]\bar{\Psi}_{\alpha E}(t) + \mathbf{H}_{\tilde{0}w}(t)e^{-iEt}\Psi^{st}_{\alpha E}$$
which is integrated numerically using any standard integration scheme.
5. The full wave function of the system is then reconstructed,
$$\Psi_{\alpha E}(t) = \bar{\Psi}_{\alpha E}(t) + e^{-iEt}\Psi^{st}_{\alpha E}.$$
6. The various observables (time-dependent current, electronic density...), which can be expressed in terms of the Lesser Green's function, are obtained by the numerical integration (and sum over incoming modes) over the energy of Eq. (22). For instance, the current between sites i and j reads,
$$I_{ij}(t) = -2\,\mathrm{Im}\sum_\alpha \int \frac{dE}{2\pi} f_\alpha(E)\Psi^*_{\alpha E}(i,t)\mathbf{H}_{ij}(t)\Psi_{\alpha E}(j,t). \tag{70}$$

7. Numerical test of the different approaches

7.1. Green's function based algorithms

Let us start the numerical applications by sending a square voltage pulse $w(t) = w_0\theta(t-t_0)\theta(t_1-t)$ inside our quantum wire ($t_1 > t_0$). Fig. 4 shows the pulse (dashed line) together with the calculation of the current $I(t)$ using the GF-C technique (red line) and WF-B (black). Our first finding is that both methods agree, which, given the fact that the two methods are totally independent, is a strong check of the robustness of the approaches. After relaxation, we expect the current to saturate to its DC value given by the Landauer formula $I_{dc} = w_0$ (transmission is unity for a perfect 1d chain), and indeed, it does. Just after the abrupt rise of the potential, one observes rapid oscillations of frequency $2\gamma/\pi$. These oscillations, often observed in numerical simulations [47], come from the fact that the rise of the voltage is (infinitely) fast compared to the bandwidth of the system, hence the band serves as a low-pass filter for the signal. Other large energy oscillations of frequency $E_F/(2\pi)$ can also be observed. The bandwidth usually corresponds to optical frequencies. For nanoelectronics applications, therefore, one should stay in a regime where the characteristic time scales of the time-dependent perturbations are large (say at least a factor 10) compared to γ^{-1}.

Before the pulse, the current vanishes. In the WF-B scheme, this is automatically encoded as the system is in a stationary state. In the GF schemes however, one needs a large value of the cut-off Δ_t to simply recover this elementary fact. The lower inset of Fig. 4 shows the current before the pulse as a function of the cut-off Δ_t together with a $1/\Delta_t$ fit. The data in the lower inset look noisy but upon closer inspection (upper inset), one finds that the convergence shows fast oscillations as $\cos(4\gamma\Delta_t)/\Delta_t$. The slow convergence of the GF schemes with respect to Δ_t is in itself a strong limitation.

As Fig. 4 considers a perfect lead, it is enough to keep a small ($N \geq 2$) number of sites in the central region. If one is interested in, say, the time it takes for a pulse to propagate, then a much larger system is necessary and GF-A becomes impractical. Fig. 5 shows a comparison between GF-B and GF-C for the calculation of the diagonal part of the Retarded Green's function for a system with $N = 100$ where the 96 central sites have been "integrated out" in order to reduce the effective size of the system. We find that the naive discretization scheme (linear multi-steps in this instance) used in GF-B fails and becomes unstable at large time while the unitarity preserving scheme of GF-C restores the stability of the algorithm. Further inspection showed that, indeed, extremely small values of h_t were needed in GF-B to enforce current conservation. GF-C is currently our best Green's function based algorithm.

7.2. Wave functions based algorithms

We now turn to the wave function based algorithms. Fig. 6 shows the local density of particles on site 1 for a system of two sites $N = 2$ using WF-A and various initial conditions. We find that the local density converges to its equilibrium value for any initial condition, and rather faster than within Green's function algorithms. More importantly, by calculating

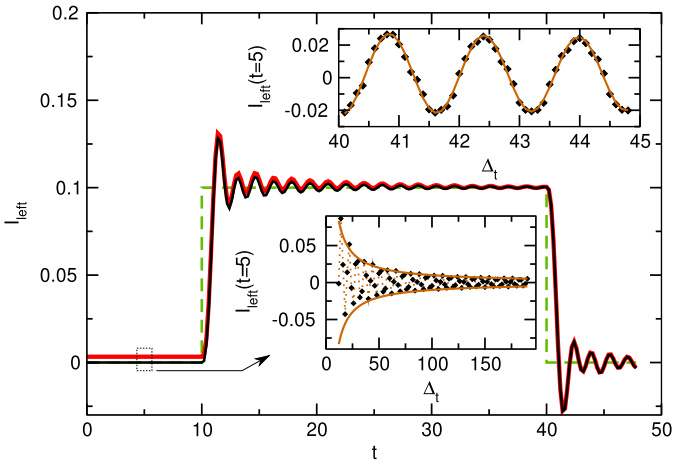

Fig. 4. Current as a function of time for a square voltage pulse $w(t) = w_0\theta(t - t_0)\theta(t_1 - t)$ with $w_0 = 0.1\gamma$, $t_0 = 10\gamma^{-1}$, $t_1 = 40\gamma^{-1}$ and $E_F = 0\gamma$. The lines show $w(t)$ (dashed), the GF-C result (red) and the WF-B result (black). Lower inset: current $I(t = 5\gamma^{-1})$ as a function of Δ_t for the GF-B scheme (symbols) together with the fit $1/\Delta_t$ (line). Upper inset: zoom of the lower inset with the fit $I = (0.1 + \cos(4\Delta_t))/\Delta_t$. (For interpretation of the references to color in this figure legend, the reader is referred to the web version of this article.)

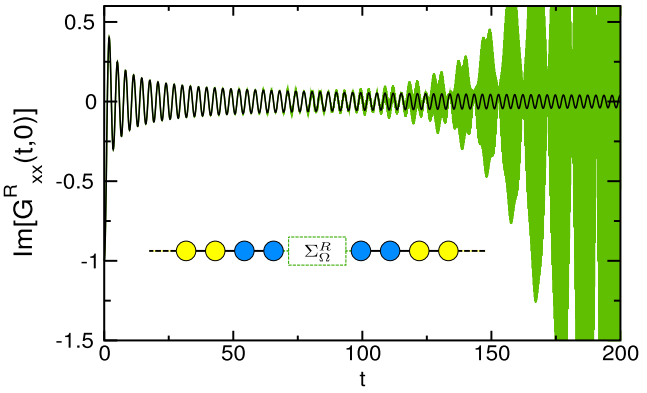

Fig. 5. Comparison of GF-B (green, divergent) and GF-C (black, stable). We plot the imaginary part of the diagonal part of the Retarded Green's function as a function of time for $N = 100$ (no time-dependent perturbation is applied). The 96 central sites have been integrated out and an effective system of four sites remains. $h_t = 0.1$. (For interpretation of the references to color in this figure legend, the reader is referred to the web version of this article.)

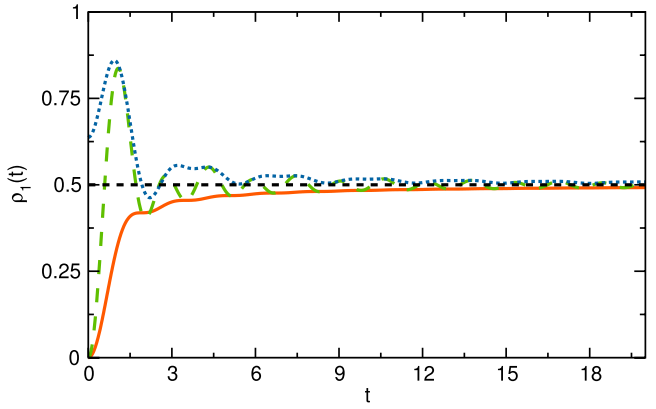

Fig. 6. Sensitivity of WF-A to initial conditions. Local density of particle on site 1 as a function of time within WF-A. The calculations are done for $\Psi_{E,x}(t = 0) = 0$ (orange full line), $\Psi_{E,x}(t = 0) = \delta_{x,1}$ (blue dotted line), $\Psi_{E,x}(t = 0) = \delta_{x,2}$ (long green dashed line) and $\Psi_{E,x}(t = 0) = \Psi_E^{st}$ (short black dashed line). Except in the last case, we ignore the memory integral for negative times. (For interpretation of the references to color in this figure legend, the reader is referred to the web version of this article.)

the DC scattering wave function (a standard object in computational DC transport), one can avoid the relaxation procedure and automatically incorporate the equilibrium properties of the system (dashed line).

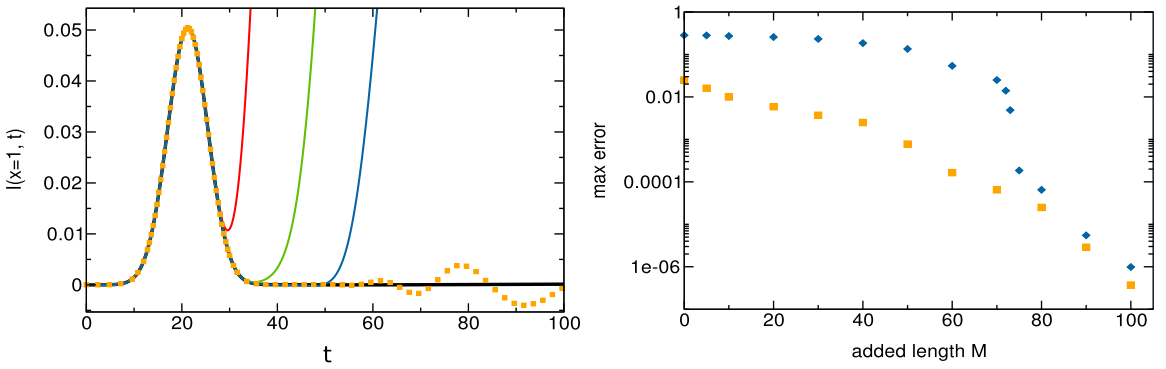

Fig. 7. Comparative study of WF-B, C and D for $N = 100$. $E_F = -1\gamma$ and we send a Gaussian voltage pulse $w(t) = V_P e^{-4\log(2)t^2/\tau_P^2}$ with $V_P = 0.05\gamma$ and $\tau_P = 10\gamma^{-1}$ through the system. Left plot: current versus time just after the voltage drop for WF-B (black), WF-C with (from left to right) $M = 10$ (red), $M = 20$ (green) $M = 30$ (blue) and WF-D $M = 30$ (orange squares). Right graph: maximum error between $t = 0\gamma^{-1}$ and $t = 100\gamma^{-1}$ as a function of M for WF-C (blue diamonds) and WF-D (orange squares). (For interpretation of the references to color in this figure legend, the reader is referred to the web version of this article.)

Table 1
Computation time in seconds for a calculation performed on a single computing core. 1D case: $N = 20$ and $t_{\max} = 10\gamma^{-1}$ (for GF-A the calculation has been done in parallel using 48 cores in order to obtain the results within a few hours). 2D case: 100×100 sites hence, $S = 100, N = 10^4$ and $t_{\max} = 100\gamma^{-1}$. The CPU time is estimated from the scaling laws except for WF-D where calculations of similar sizes could be performed. Third column: typical scaling of the computing time. A notable additional difference between the WF and GF methods is that (*) the GF methods only provide the observables at one given time per calculation while the WF methods give the full curve in one run. Typical values of N_E needed for the integrations over energy are $20 < N_E < 100$.

Algorithm	CPU (1D)	Estimated CPU (2D)	Scaling of CPU
WF-D	1	10^4	$(t/h_t)N_E[N + \gamma tS]$
WF-B	40	4.10^7	$(t/h_t)N_E[N + (t/h_t)S^2]$
GF-C	10^4	10^{12}	$(t/h_t)^2S^3$ (*)
GF-A	10^5	10^{14}	$(t/h_t)^2S^2N$ (*)

WF-B which naturally captures the equilibrium conditions is a clear improvement over WF-A. According to the arguments developed above, WF-C and D should permit further improvements. Upper Fig. 7 shows current versus time in presence of a Gaussian pulse for the three methods WF-B, C and D (and various values of the number M of added sites for the latter two). In the case of WF-C, one observes a very accurate regime until a time $t_0 \propto M$ where the method abruptly becomes very inaccurate. This is due to the finiteness of the effective system in WF-C. t_0 corresponds to the time it takes for the signal to travel until the end of the sample and back again after being reflected at the end. The wide band limit approximation used in WF-D allows one to limit this abrupt failure and results in a much more robust (and slightly faster) method. Lower Fig. 7 shows the (maximum) error made as a function of M. As surmised, very small values of M are needed for very accurate results. WF-D is our fastest and most robust method.

7.3. *Relative performance of the different approaches*

We end this section with Table 1 that compares the relative performance of the various methods presented here. We find that WF-D is now fast enough to study two or three dimensional systems with tens of thousand of sites (work station) or millions of sites (supercomputers) with matching simulation times. More applications will be shown later in the text and will show that WF-D essentially bridges the gap between our simulation capabilities for stationary problems and time-dependent ones.

Table 1 shows rather unambiguously the superiority of the WF-D approach over all the others, especially the GF approaches. GF-B (not stable for long times, otherwise similar to GF-C), WF-A (similar to WF-B but much less robust) and WF-C (similar to WF-D but less robust and slightly slower) are not shown. Note that the given times correspond to single core calculations. WF-D can be further accelerated using two levels of parallelism: a trivial one is the calculation of different energies on different cores (allowing to drop the factor N_E). The second one is the sparse matrix - dense vector multiplication in the evaluation of the product $\mathbf{H}_{\bar{0}\bar{0}}(t)\bar{\Psi}_{\alpha E}(t)$ in Eq. (33). There are also two avenues for optimization which were not yet explored in depth: the choice of the time integration scheme (e.g. an adaptive time step) and the choice of the scheme for the integration over energy (here again a combination of Gaussian quadrature scheme with an adaptive energy mesh might be more effective than a naive approach).

8. A Landauer formula for voltage pulses

So far, the formalism and numerical techniques that have been presented are applicable to arbitrary time-dependent perturbations. We now proceed with the particular case where the perturbation is a pulse of finite duration.

8.1. Total number of injected particle

We aim to define the generalization of the Landauer formula for pulse physics. A natural extension would be to compute the time-dependent current $I_{\bar{p}}(t)$ in lead $\bar{p}$. It is given by,

$$I_{\bar{p}}(t) = \int \frac{dE}{2\pi} \sum_{\alpha} f_{\alpha}(E) I_{\alpha E,\bar{p}}(t) \tag{71}$$

with

$$I_{\alpha E,\bar{p}}(t) = 2\, Im\, \Psi^{\dagger}_{\alpha E,\bar{p}x}(t) V^{\dagger}_{\bar{p}} \Psi_{\alpha E,\bar{p}x-1}(t) \tag{72}$$

the notation corresponding to that introduced in the scattering matrix Section 5. We can now insert Eq. (40) into the definition of $I_{\bar{p}}(t)$ and to express it in terms of the scattering matrix. The general formula involves a triple integral over energy which is not very illuminating. It also lacks the basic properties of the Landauer–Buttiker approach which arise from current conservation (time-dependent current is not conserved) and gauge invariance. An important simplification occurs when one calculates the total number of particles $n_{\bar{p}} = \int_0^{t_M} dt I_{\bar{p}}(t)$ received in lead p in the limit $t_M \to \infty$. Of course, at this level of generality, $n_{\bar{p}}$ can possibly diverge due to the presence of DC currents. Hence, the following expressions assume a finite (large) value of the cutoff t_M. Introducing $n_{\alpha E,\bar{p}} = \int_0^{t_M} dt\, I_{\alpha E,\bar{p}}(t)$, we obtain

$$n_{\alpha E,\bar{p}} = \sum_{\beta\in\bar{p}} \int \frac{dE'}{2\pi} P_{\bar{p}\beta,\bar{m}\alpha}(E',E) - \int_0^{t_M} dt\, \delta_{\alpha\beta}\delta_{\bar{p}\bar{m}}. \tag{73}$$

$$\lim_{t_M\to\infty} P_{\bar{p}\beta,\bar{m}\alpha}(E',E) = |S_{\bar{p}\beta,\bar{m}\alpha}(E',E)|^2. \tag{74}$$

$P_{\bar{p}\beta,\bar{m}\alpha}(E',E)$ is thus interpreted as the probability density to be scattered from channel α and energy E to channel β and energy E'. Equivalently, introducing the Fourier transform $S_{\bar{p}\beta,\bar{m}\alpha}(t,E) \equiv \int \frac{dE'}{2\pi} e^{-iE't} S_{\bar{p}\beta,\bar{m}\alpha}(E',E)$ and using Parseval theorem, one obtains

$$n_{\alpha E,\bar{p}} = \sum_{\beta\in\bar{p}} \int_0^{t_M} dt\, [P_{\bar{p}\beta,\bar{m}\alpha}(t,E) - \delta_{\alpha\beta}] \tag{75}$$

$$\lim_{t_M\to\infty} P_{\bar{p}\beta,\bar{m}\alpha}(t,E) = |S_{\bar{p}\beta,\bar{m}\alpha}(t,E)|^2. \tag{76}$$

As the wave function $\Psi_{\alpha E}$ obeys the Schrödinger equation, one gets a current conservation equation $\partial_t Q_{\alpha E,\bar{0}} = \sum_{\bar{p}} I_{\alpha E,\bar{p}}(t)$ where $Q_{\alpha E,\bar{0}} = \Psi_{\alpha E}(t)^{\dagger}\Psi_{\alpha E}(t)$ is the total number of particle inside the system associated with mode α and energy E. Long after the pulse, the system is back to equilibrium so that $Q_{\alpha E,\bar{0}}(t_M) = Q_{\alpha E,\bar{0}}(0)$ and the current conservation implies,

$$\forall E,\ \forall\alpha\ \sum_{\bar{p}} n_{\alpha E,\bar{p}} = 0. \tag{77}$$

Putting everything together, we obtain,

$$n_{\bar{p}} = \sum_{\bar{m}} \sum_{\alpha\in\bar{m}} \int \frac{dE}{2\pi} f_{\bar{m}}(E) n_{\alpha E,\bar{p}}. \tag{78}$$

To summarize, we find a formal analogy between the known rules of conventional (DC) scattering theory and those of time-dependent transport. Summations over channels are extended to a summation over channels *and* an integral over energy (or time) while the current is replaced by the total number of transmitted particles. In practice, the different terms contributing to $n_{\bar{p}}$ should be grouped in such a way that the limit $t_M \to \infty$ can be taken without divergences (in the absence of DC current).

8.2. Scattering matrix of a voltage pulse

The theory above is rather general. We proceed with the particular case where the perturbation is a voltage pulse applied to one electrode. We consider an abrupt voltage drop across an infinite wire described by the Hamiltonian matrix (5). The

voltage drop takes place between layers $x = 0$ and $x = 1$. For this system, the Scattering matrix has a block structure in terms of the reflection r and transmission d amplitude,

$$S_{\beta\alpha}(E', E) = \begin{pmatrix} r_{\beta\alpha}(E', E) & d_{\beta\alpha}(E', E) \\ d'_{\beta\alpha}(E', E) & r'_{\beta\alpha}(E', E) \end{pmatrix} \tag{79}$$

which corresponds to the following form of the scattering wave function,

$$x > 0: \psi_x^{scatt}(t) = \psi_x^d(t), \qquad x \leq 0: \psi_x^{scatt}(t) = \psi_x^r(t) \tag{80}$$

with

$$\psi_x^r(t) = \frac{\xi^+_{\bar{m}\alpha}(E)}{\sqrt{|v^+_{\bar{m}\alpha}|}} e^{-iEt+ik^+_\alpha(E)x} + \sum_\beta \int \frac{dE'}{2\pi} \frac{\xi^-_{\bar{m}\beta}(E')}{\sqrt{|v^-_{\bar{m}\beta}|}} e^{-iE't-ik^-_\beta(E')x} r_{\beta\alpha}(E', E) \tag{81}$$

$$\psi_x^d(t) = \sum_\beta \int \frac{dE'}{2\pi} \frac{\xi^+_{\bar{m}\beta}(E')}{\sqrt{|v^+_{\bar{m}\beta}|}} e^{-iE't+ik^+_\beta(E')x} d_{\beta\alpha}(E', E) \tag{82}$$

where the subscript $+$ $(-)$ refers to right (left) going modes. $\psi_x^r(t)$ and $\psi_x^d(t)$ satisfy $i\partial_t\psi_x(t) = H_{\bar{m}}\psi_x(t) + V^\dagger_{\bar{m}}\psi_{x-1}(t) + V_{\bar{m}}\psi_{x+1}(t)$ for all values of x while $\psi_x^{scatt}(t)$ satisfies the "matching conditions",

$$i\partial_t\psi_0^{scatt}(t) = H_{\bar{m}}\psi_0^{scatt}(t) + V^\dagger_{\bar{m}}\psi_{-1}^{scatt}(t) + V_{\bar{m}}e^{i\phi_{\bar{m}}(t)}\psi_{+1}^{scatt}(t) \tag{83}$$

$$i\partial_t\psi_1^{scatt}(t) = H_{\bar{m}}\psi_1^{scatt}(t) + V^\dagger_{\bar{m}}e^{-i\phi_{\bar{m}}(t)}\psi_0^{scatt}(t) + V_{\bar{m}}\psi_{+2}^{scatt}(t) \tag{84}$$

from which we directly get

$$V_{\bar{m}}\psi_1^r(t) = V_{\bar{m}}e^{i\phi_{\bar{m}}(t)}\psi_1^d(t) \tag{85}$$

$$V^\dagger_{\bar{m}}\psi_0^r(t) = V^\dagger_{\bar{m}}e^{i\phi_{\bar{m}}(t)}\psi_0^d(t). \tag{86}$$

Inserting the explicit forms of $\psi_x^r(t)$ and $\psi_x^d(t)$ into Eqs. (85) and (86) (and making use of Eqs. (36) and (37)), we obtain the equation satisfied by the transmission matrix,

$$\sum_\beta \int \frac{dE'}{2\pi} K_{\bar{m}}(\epsilon - E') \left[\Sigma^R_{\bar{m}}(E') - \Sigma^R_{\bar{m}}(\epsilon)^\dagger\right] \frac{\xi^+_{\bar{m}\beta}(E')}{\sqrt{|v^+_{\bar{m}\beta}(E')|}} d_{\beta\alpha}(E', E) = \left[\Sigma^R_{\bar{m}}(E) - \Sigma^R_{\bar{m}}(\epsilon)^\dagger\right] \frac{\xi^+_{\bar{m}\alpha}(E)}{\sqrt{|v^+_{\bar{m}\alpha}(E)|}} 2\pi\delta(\epsilon - E) \tag{87}$$

and similarly

$$\sum_\beta \int \frac{dE'}{2\pi} K^*_{\bar{m}}(E' - \epsilon) \left[\Sigma^R_{\bar{m}}(E') - \Sigma^R_{\bar{m}}(\epsilon)^\dagger\right] \frac{\xi^-_{\bar{m}\beta}(E')}{\sqrt{|v^-_{\bar{m}\beta}(E')|}} d'_{\beta\alpha}(E', E) = \left[\Sigma^R_{\bar{m}}(E) - \Sigma^R_{\bar{m}}(\epsilon)^\dagger\right] \frac{\xi^-_{\bar{m}\alpha}(E)}{\sqrt{|v^-_{\bar{m}\alpha}(E)|}} 2\pi\delta(\epsilon - E) \tag{88}$$

where $K_{\bar{m}}(E)$ is the harmonic content of the voltage pulse,

$$K_{\bar{m}}(E) = \int dt\, e^{i\phi_{\bar{m}}(t)+iEt}. \tag{89}$$

In the situation where time-reversal symmetry is present $\mathbf{H}_{\bar{m}\bar{m}} = \mathbf{H}^*_{\bar{m}\bar{m}}$ (no spin), one finds that to each right-going mode $\xi^+_{\bar{m}\alpha}$ is associated a left-going one $(\xi^+_{\bar{m}\alpha})^*$ with equal velocity. It follows that

$$d'_{\beta\alpha}(E', E) = d_{\beta\alpha}(E, E')^*. \tag{90}$$

The relation between left and right propagating modes is however more complex in presence of magnetic field. We continue with a physical assumption, namely that the typical pulse height (w_p) is small compared to the Fermi energy $w_P \ll E_F$. We also suppose that its duration τ_P is rather long, $\hbar/\tau_P \ll E_F$. This is in fact the typical situation in actual experiments where the Fermi level $E_F \approx 1$ eV (metal) or $E_F \approx 10$ meV (semi-conductor heterostructure) is much larger than the typical characteristic energies of the pulses ($w_P < 1\,\mu$eV, $\tau_P \approx 1$ ns $\to \hbar/\tau_P \approx 1\,\mu$eV). As the kernel $K_{\bar{m}}(E)$ typically decays over $\max(w_P, \hbar/\tau_P)$, we can therefore neglect the energy dependence of the modes in Eq. (87) (the so called wide band limit) which are all taken to be at energy E. The terms $\Sigma^R_{\bar{m}}(E') - \Sigma^R_{\bar{m}}(\epsilon)^\dagger$ simplify into $\Sigma^R_{\bar{m}}(E) - \Sigma^R_{\bar{m}}(E)^\dagger = -i\Gamma_{\bar{m}}(E)$ and Eq. (39) leads to

$$d_{\beta\alpha}(E', E) = \delta_{\alpha\beta}K^*_{\bar{m}}(E - E') \tag{91}$$

or

$$d_{\beta\alpha}(t, E) = \delta_{\alpha\beta}e^{-i\phi_{\bar{m}}(t)-iEt} \tag{92}$$

while $d'_{\beta\alpha}(E, E') = \delta_{\alpha\beta}K_{\bar{m}}(E' - E)$. We note that in the wide band limit Eq. (90) holds even in the presence of magnetic field. Also, the reflection matrix $r_{\beta\alpha}(E', E)$ simply vanishes in this limit. The role of the voltage drop is therefore purely to redistribute the energy of the incoming electron into a larger energy window.

8.3. Voltage pulses in multiterminal systems

We now have all the ingredients to construct the theory of voltage pulses in general multiterminal systems. We assume that before the pulse, the system is at equilibrium with no DC current flowing. We also assume the wide band limit of the above section, which implies that all the inelastic processes of the scattering matrix take place at the position of the voltage drop. The assumption that no reflection takes place at this place is important as each electron experiences at most two inelastic events (upon entering and leaving the sample) which considerably simplifies the theory. Introducing the DC scattering matrix $S^0_{\bar{p}\beta,\bar{m}\alpha}(\epsilon)$ of the device *in the absence of pulses*, we have

$$S_{\bar{p}\beta,\bar{m}\alpha}(E',E) = \int \frac{d\epsilon}{2\pi} K_{\bar{p}}(\epsilon - E')\, S^0_{\bar{p}\beta,\bar{m}\alpha}(\epsilon)\, K^*_{\bar{m}}(E-\epsilon). \tag{93}$$

Using $\int dE/(2\pi) K_{\bar{m}}(\epsilon - E) K^*_{\bar{m}}(\bar{\epsilon} - E) = 2\pi\delta(\bar{\epsilon} - \epsilon)$, we find upon performing the integral over E' in Eq. (73)

$$n_{\bar{p}} = \sum_{\bar{m}} \sum_{\beta\in\bar{p}} \sum_{\alpha\in\bar{m}} \int \frac{d\epsilon}{2\pi} \left[\int \frac{dE}{2\pi} f(E) |S^0_{\bar{p}\beta,\bar{m}\alpha}(\epsilon)|^2\, |K_{\bar{m}}(E-\epsilon)|^2 - f(\epsilon) \int_0^{t_M} dt\; \delta_{\alpha\beta}\delta_{\bar{p}\bar{m}} \right]. \tag{94}$$

By using the unitarity of the device Scattering matrix $\sum_{\bar{m}\beta} |S^0_{\bar{p}\beta,\bar{m}\alpha}(\epsilon)|^2 = \delta_{\alpha\beta}\delta_{\bar{p}\bar{m}}$ in the second part of Eq. (94), it can be rewritten in a more compact form where the limit $t_M \to \infty$ can be taken formally. It reads,

$$\begin{aligned} n_{\bar{p}} &= \sum_{\bar{m}} N_{\bar{p}\bar{m}} \\ N_{\bar{p}\bar{m}} &= \sum_{\beta\in\bar{p}} \sum_{\alpha\in\bar{m}} \int \frac{d\epsilon}{2\pi} |S^0_{\bar{p}\beta,\bar{m}\alpha}(\epsilon)|^2 \int \frac{dE}{2\pi} |K_{\bar{m}}(E-\epsilon)|^2 \left[f(E) - f(\epsilon) \right]. \end{aligned} \tag{95}$$

Eq. (95) is the main result of this section. The "pulse conductance matrix" $N_{\bar{p}\bar{m}}$ can be seen as the formal generalization of the multiterminal DC conductance matrix [78] to voltage pulses. In particular it shares two important properties of the DC conductance matrix: charge conservation and gauge invariance. Eqs. (94) and (95) call for a number of comments. In particular they consist of the difference of two large terms so that some care is needed when performing practical calculations.

- First, Eq. (94) contains a diverging term on the right hand side which corresponds to the injected current from lead $\bar{m}$. Indeed, at equilibrium, although the net total currents coming from the different leads cancel, each lead injects a finite current, leading to a diverging number of injected particles. Therefore, to use Eq. (94) in practice, it is important to first sum the contribution from all leads before performing the integrals. Also, one must add those contributions at fixed energy ϵ (i.e. the energy inside the device region, not E the original energy of the injected particle) for those diverging terms to properly compensate.
- Second, although Eq. (94) apparently contains contributions from the whole spectrum, one can show that the only non-compensating terms arise from a small region around the Fermi energy. Indeed, let us consider an energy ϵ well below E_F. The kernel $K_{\bar{m}}(E-\epsilon)$ vanishes when $E-\epsilon$ becomes larger than $\max(w_P, \hbar/\tau_P)$ so that the values of E effectively contributing to the integral are also well below E_F, hence $f(E) = f(\epsilon) = 1$. The integral over the energy E can now be performed and, using Parseval theorem, we get $\int dE |K_{\bar{m}}(E-\epsilon)|^2 = \int_0^{t_M} dt$. We can now sum over the channel index α and lead index $\bar{m}$ using the unitarity condition $\sum_{\alpha\bar{m}} |S^0_{\bar{p}\beta,\bar{m}\alpha}(\epsilon)|^2 = 1$ and finally find that the first term of Eq. (94) compensates the second one for each energy ϵ. Again, to obtain this compensation it is important to *first* perform the integral over the injected energy E at fixed energy ϵ. The same point applies to Eq. (95): E and ϵ must be close for $K_{\bar{m}}(E-\epsilon)$ to be non zero hence the term $f(E) - f(\epsilon)$ vanishes away from the Fermi level. More discussion on this aspect can be found around Fig. 15.
- Current conservation is one of the main features of the Landauer approach which is usually lost in non-interacting AC transport, as the electronic density varies in time inside the system [12]. However the total number of particles is a conserved quantity and

$$\sum_{\bar{p}} N_{\bar{p}\bar{m}} = 0 \tag{96}$$

  as can be seen directly on Eqs. (94), (95) or from the general argument at the beginning of this section.
- Another equally important feature of the scattering approach is the gauge invariance – raising the potential of all the leads simultaneously does not create any current – which is also usually lost in the non-interacting AC theory. However Eq. (94) does satisfy gauge invariance. Indeed, suppose we send an identical voltage pulse on all the leads simultaneously. Then the term $|K_{\bar{m}}(E-\epsilon)|^2$ does not depend on $\bar{m}$ and one can immediately perform the sum over α and $\bar{m}$ and use $\sum_{\alpha\bar{m}} |S^0_{\bar{p}\beta,\bar{m}\alpha}(\epsilon)|^2 = 1$. In a second step we perform the integral over E of the first term of Eq. (94) using Parseval theorem and find again that it exactly matches and compensates the second term and $n_{\bar{p}} = 0$. Note that while the above statement is non trivial, there is a weaker form of gauge invariance which is always verified: the physics is entirely unaffected by

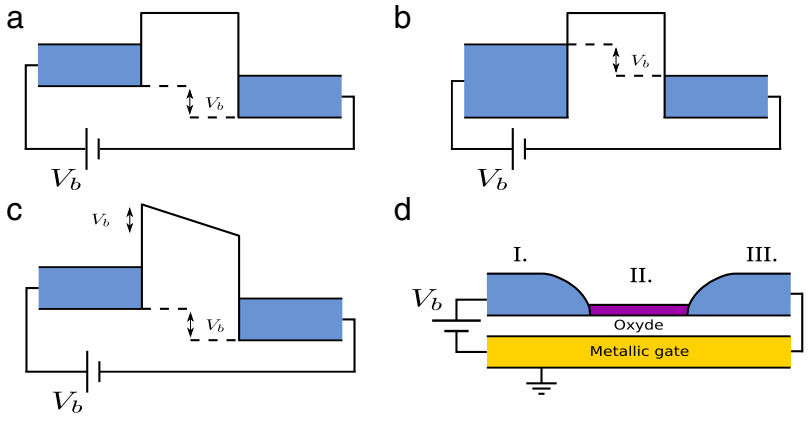

Fig. 8. Sketch of different repartitions between chemical and electrical potential upon applying a difference of electrochemical potential V_b between source and drain. (a) Abrupt drop of purely electrical nature. (b) The drop is purely of chemical nature. (c) The purely electric drop takes place linearly over the sample (tunnel junction situation). (d) Device corresponding to case (a): the two electrodes I and III correspond to regions with high density of states while the central region II has a low density of states. A metallic gate, at a distance d below the sample, screens the charges present in the sample.

a global change of the potentials of all the leads *and* the internal potential of the device (as such a global variation of the potential can be absorbed by a simple global phase in the wave function). The combination of both forms of gauge invariance (weak and strong) implies that a uniform voltage pulse applied to the central region $\bar{0}$ (through a capacitive coupling to a gate) does not create any charge pumping, even in the non adiabatic limit.

- One of the appealing aspects of Eq. (95) is that it has a direct connection to the DC conductance matrix in the adiabatic limit. Indeed the DC Landauer formula reads,

$$I_{\bar{p}} = \frac{e^2}{h} \sum_{\bar{m}} T_{\bar{p}\bar{m}} V_{\bar{m}} \tag{97}$$

where $T_{\bar{p}\bar{m}}$ is the total transmission probability from lead $\bar{m}$ to $\bar{p}$. When the voltage pulse is extremely slow (adiabatic limit) with respect to all the characteristic times of the device, one expects the current to follow the voltage adiabatically, $I_{\bar{p}}(t) = (e^2/h) \sum_{\bar{m}} T_{\bar{p}\bar{m}} V_{\bar{m}}(t)$ and

$$n_{\bar{p}} = \sum_{\bar{m}} T_{\bar{p}\bar{m}} \bar{n}_{\bar{m}} \tag{98}$$

where $\bar{n}_{\bar{m}} = \int dt e V_{\bar{m}}(t)/h$ is the total number of particles *injected* by the voltage pulse in lead $\bar{m}$. Hence, in the adiabatic limit, $N_{\bar{p}\bar{m}} = T_{\bar{p}\bar{m}} \bar{n}_{\bar{m}}$ has a nice interpretation in terms of the total transmission probability from $\bar{m}$ to $\bar{p}$ and the interesting question is how the physics deviates from this limit when the pulses get faster than the internal characteristic time scales of the device.

8.4. A comment on the electrostatics

We end this section with a discussion of our choice of boundary conditions in the electrodes and our model for an abrupt voltage drop. Following the usual practice [47], we have assumed (i) that the voltage drops abruptly at the electrode – system interface and (ii) that the electrodes remain at thermal equilibrium (in the basis where the gauge transformation has been performed so that the electrode Hamiltonian is time-independent). Conditions (i) and (ii) correspond to case (a) in Fig. 8; an abrupt drop of the electrical potential at the lead – system interface. In an actual experiment, however, a voltage source does not impose a difference of electric potential but rather a difference of *electrochemical* potential. How the latter is split between electric and chemical potential is a matter of the balance between the electrostatic and chemical (i.e. kinetic) energy of the system and is therefore extrinsic to the model discussed so far. Fig. 8(b) and (c) illustrate two possible ways of splitting these contributions. In the former case the potential drop is of a purely chemical nature, whereas in the latter the potential drop is purely electrical and is not abrupt.

Note that our model, Fig. 8(a), implies a small potential mismatch at the electrode — system interface which in turn induces a finite reflection amplitude, which is not the case in Fig. 8(b). For DC current with small bias both models coincide, but differences occur at large biases. Fig. 9 shows the stationary value of the current after a fast increase of the voltage. We use a pulse of form $w(t) = V\theta(t)$, wait for a long ($t = 100$) time after the voltage has been established and compute the corresponding stationary current (using any of the above equivalent methods, in this case GF-A). One can check from Fig. 4 that $t = 100$ is sufficient to achieve convergence toward the stationary value. This can be considered as a very elaborate (and ineffective) way to obtain the $I(V)$ characteristics of the device. We also calculated directly the DC $I(V)$ characteristics using the stationary equations [74] and checked that we obtained matching results. Fig. 9 shows two curves. The first curve,

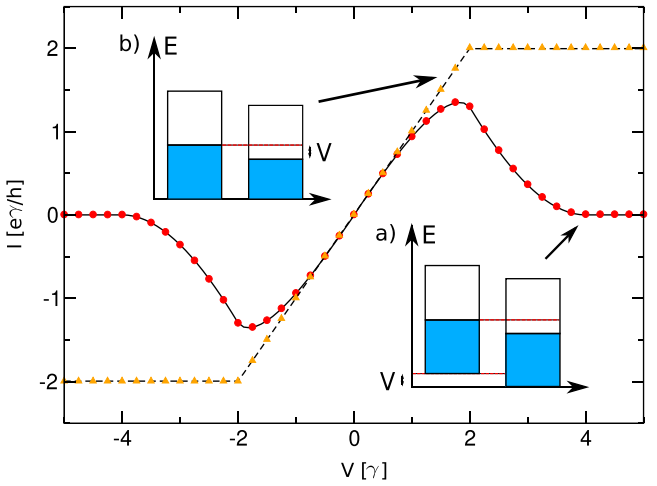

Fig. 9. $I(V)$ characteristics of the 1D chain. Symbols: results obtained with GF-A after a fast voltage rise $w(t) = V\theta(t)$ and letting the system equilibrate for $t = 100\gamma^{-1}$. Lines: corresponding pure DC calculation. We compare the case (a) where the drop of potential is purely electric (triangles, choice made everywhere else in this article) and (b) where it is purely chemical (circles). Inset, schematic of the corresponding adjustments of the band positions and Fermi levels. The shaded blue region corresponds to the filled states of the band.

Fig. 9(a): red circles, corresponds to the natural condition in our formalism (case Fig. 8(a)). The voltage drop is a drop of *electric* potential, hence there is a corresponding shift of the band of the left lead with respect to the right one. The second curve, Fig. 9(b): triangles, corresponds to a change of *chemical* potential (Fig. 8(b)), the bottom of the right and left bands remain aligned. When V becomes large compared to the Fermi energy the two prescriptions differ; a drop of electric voltage implies backscattering while in (b) the transmission probability is always unity. Also, a current in (a) implies that the bands in the two leads overlap which does not happen when V is larger than the bandwidth of the system. At large V the current therefore saturates to $2e\gamma/h$ in (b) while it vanishes in (a).

While a full discussion of the electrostatics lies out of the scope of the present paper, let us briefly discuss a simple situation which clarifies which boundary condition is the most appropriate for a given situation. A sketch of the system is given in Fig. 8(d). It consists of two metallic electrodes I and III with a high electronic density of states (per unit area) ρ_I and ρ_{III} connected to a central device region with lower density of states ρ_{II} (typically a GaAs/AlGaAs heterostructure or a graphene sheet). Underneath the system, at a distance d, is a metallic gate which is grounded. In a typical measurement setup the electrode III is grounded while a voltage source V_b is placed between the electrode I and the metallic gate. Upon imposing the electrochemical potential eV_b in region I, a variation U_I (μ_I) of electric (chemical) potential takes place with $eV_b = eU_I + \mu_I$. The variation of chemical potential corresponds to a variation of electronic density $n_I = \rho_I\mu_I$ (quantum capacitance). On the other hand, the presence of the underlying gate corresponds to an electric capacitance (per unit area) $C = \epsilon/d$ and the electrostatic condition reads $n_I = CU_I/e$. Putting everything together we arrive at

$$U = \frac{V_b}{1 + C/(e^2\rho_I)}. \tag{99}$$

Turning to concrete examples, we find that for typical transition metals (very high density of states) $U \approx V_b$ as raising the chemical potential would imply a huge increase in the density which in turn would induce a correspondingly large increase in the electrostatic energy. Metallic electrodes are thus typically associated to the cases of Fig. 8(a) or (c). The behavior in region II depends acutely on ρ_{II}. If the density of states in region II is high enough (say a 2D gas with a screening gate at $d = 100$ nm) then the electric potential decays linearly from eV_b (region I) to 0 (region III), as shown in Fig. 8(c). If the density of states in region II is small, however, (e.g. one dimensional systems such as edge states in the Quantum Hall regime or a carbon nanotube) the ratio $C/(e^2\rho_I)$ becomes large and U_{II} vanishes [case Fig. 8(a)]. We conclude that while the situation depicted in Fig. 8(b) is fairly rare (although possible using for instance a graphene electrode coupled through a BN layer to an extremely close underlying graphene gate), the situation of Fig. 8(a), which is the focus of this paper, is typical of a mesoscopic system. In this case, the drop of the electric potential will typically take place over a distance d. While the simulation of case (a) and (c) is straightforward within our formalism, case (b) (fortunately often not realistic) would require additional extrinsic inputs. While the electric potential adjusts itself instantaneously (i.e. at the speed of light) inside the sample, the chemical potential propagates at the group velocity of the electrons, and a proper model of the inelastic relaxation inside the electrodes would be necessary.

9. A pedestrian example: propagation and spreading of a voltage pulse inside a one dimensional wire

While most elementary courses on quantum mechanics concentrate on the stationary limit, one aspect of the time-dependent theory stands out: the spreading of a (mostly Gaussian) wave packet. An initial wave packet with a certain spatial

width and average momentum experiences a ballistic motion of its center of mass while its width spreads diffusively. The spreading of the wave packet provides a simple illustration of a central concept of quantum mechanics, the Heisenberg principle between time and energy. In this section, we study a case which can be considered as the condensed matter analogue of the spreading of the wave packet: the propagation and spreading of an initial condition which is given in terms of a voltage pulse. The voltage pulse shares some similarities with the usual "localized wave packet", yet there are also important differences. In particular, in an electronic system, there are stationary delocalized waves which exist before the pulse. Hence, a voltage pulse does not create a localized wave packet but a local deformation of (mostly the phase of) an existing one.

The main result of this section is that the spreading of a voltage pulse is accompanied by density (and current) oscillations that follow the propagation of the pulse. The sort of wake which is formed by these oscillations is unfortunately mainly of academic interest as its experimental observation appear to be extremely difficult.

We start this section with a pedestrian construction of the scattering matrix of a one dimensional chain. We then leave the discrete model for the continuous limit which is more tractable analytically. We end this section with an explicit calculation of the spreading of the wave packet and the above mentioned wake that follows the ballistic propagation of the pulse.

9.1. Scattering matrix: analytics

Our starting point is the Schrödinger equation for the one dimensional chain (i.e. the first quantization version of Hamiltonian (62) with a static potential $\epsilon_i = 2\gamma$ over the entire infinite chain),

$$i\partial_t \psi_x = -\gamma\psi_{x-1} - \gamma\psi_{x+1} + 2\gamma\psi_x, \quad \forall x \neq 0, 1 \tag{100}$$

$$i\partial_t \psi_0 = -\gamma\psi_{-1} - e^{i\phi(t)}\gamma^t\psi_1 + 2\gamma\psi_0, \tag{101}$$

$$i\partial_t \psi_1 = -\gamma\psi_2 - e^{-i\phi(t)}\gamma^t\psi_0 + 2\gamma\psi_1, \tag{102}$$

where the hopping element γ_t between sites 0 and 1 can be different from the hopping γ of the rest of the system. As the time-dependent part of the Hamiltonian concentrates on a single hopping term between sites 0 and 1, we can build the states on either side with a linear combination of the plane waves of the system,

$$\psi_x = \frac{e^{-iEt+ik(E)x}}{\sqrt{|v(E)|}} + \int \frac{dE'}{2\pi}\frac{e^{-iE't-ik(E')x}}{\sqrt{|v(E')|}} r(E', E), \quad \forall x \leq 0 \tag{103}$$

$$\psi_x = \int \frac{dE'}{2\pi}\frac{e^{-iE't+ik(E')x}}{\sqrt{|v(E')|}} d(E', E), \quad \forall x \geq 1 \tag{104}$$

with $E(k) = 2\gamma(1 - \cos k)$ and $v = \partial E/\partial k$. The "wave-matching" conditions Eqs. (101) and (102) translate, for our ansatz, into

$$\frac{e^{-ik(E')}}{\sqrt{|v(E')|}} r(E', E) + 2\pi\frac{e^{ik(E)}}{\sqrt{|v(E)|}}\delta(E' - E) = (\gamma^t/\gamma)\int \frac{d\epsilon}{2\pi} K(E' - \epsilon)\frac{e^{ik(\epsilon)}}{\sqrt{|v(\epsilon)|}} d(\epsilon, E) \tag{105}$$

$$\frac{1}{\sqrt{|v(E')|}} d(E', E) = (\gamma^t/\gamma)\left[\frac{1}{\sqrt{|v(E)|}} K^*(E - E') + \int \frac{d\epsilon}{2\pi} K^*(\epsilon - E')\frac{1}{\sqrt{|v(\epsilon)|}} r(\epsilon, E)\right] \tag{106}$$

Eqs. (105) and (106) can be solved systematically, order by order, in power of γ^t/γ. The first non vanishing term for the transmission reads,

$$d(E', E) = (\gamma^t/\gamma)\sqrt{\frac{v(E')}{v(E)}}[1 - e^{2ik(E)}]K^*(E - E') + O(\gamma^t/\gamma)^2. \tag{107}$$

Of course, Eqs. (105) and (106) can also be solved in the wide band limit, as in the previous section. The wide band limit leads to,

$$r(t, E)e^{-ik(E)} + e^{ik(E)}e^{-iEt} = (\gamma^t/\gamma)e^{i\phi(t)}e^{ik(E)}d(t, E) \tag{108}$$

$$d(t, E) = (\gamma^t/\gamma)e^{-i\phi(t)}\left[e^{-iEt} + r(t, E)\right] \tag{109}$$

from which we get,

$$d(t, E) = (\gamma^t/\gamma)e^{-i\phi(t)}e^{-iEt}\frac{e^{ik(E)} - e^{-ik(E)}}{(\gamma^t/\gamma)e^{ik(E)} - e^{-ik(E)}} \tag{110}$$

which is a simple generalization (for $\gamma^t \neq \gamma$) of the result derived in the previous section. For $\gamma^t = \gamma$ one obtains $d(E', E) = K^*(E - E')$.

Let us now briefly look at the shape of the transmitted wave that can be reconstructed from the knowledge of $d(E', E)$ and Eq. (104). In the wide band limit $E(k') = E(k)$, it reads,

$$\psi(x,t) = \frac{1}{\sqrt{v}} e^{-iEt} e^{ikx} e^{i\phi(t)}. \tag{111}$$

We find that in this solution the pulse does not propagate, which is to be expected as the wide band limit neglects the system velocity. Using a linear dispersion $E(k') = E(k) + v(k' - k)$ improves the situation as the corresponding wave function,

$$\psi(x,t) = \frac{1}{\sqrt{v}} e^{ikx - iEx/v} d(t - x/v) \tag{112}$$

shows the ballistic propagation of the pulse. In the limit where the velocity of the wave is slow (with respect to the typical scales of the voltage pulse) one can use $d(t) = e^{-i\phi(t) - iEt}$,

$$\psi(x,t) = \frac{1}{\sqrt{v}} e^{ikx - iEt} e^{-i\phi(t - x/v)}. \tag{113}$$

At this level of approximation the voltage pulse can be considered as a "phase domain wall" which propagates ballistically inside the wire. The spreading of the voltage pulse is associated to the mass of the particle, i.e. to the curvature of the dispersion relation, and therefore is beyond the linear dispersion considered here. Also, the expression $d(t - x/v) = e^{-i\phi(t - x/v)}$ is slightly ill-defined as it does not fulfill particle conservation (it corresponds to a uniform density yet a non uniform current). This reflects the fact the transmission matrix itself was calculated in the wide band limit, i.e. without taking the electronic propagation into account.

We continue by taking the continuum limit of the problem, i.e. we introduce a small discretization step a, set $\gamma = \hbar^2/(2ma^2)$ and $k \to ka$. The limit $a \to 0$ provides the usual quadratic dispersion of the Schrödinger equation, $E(k) = \hbar^2 k^2/(2m)$. In this limit, we can solve Eqs. (105) and (106) for a linear spectrum, beyond the wide band limit. We obtain,

$$\dot{r} - iEr + 2iEe^{-iEt} = (\gamma^t/\gamma) e^{i\phi(t)} [iEd - \dot{d}] \tag{114}$$

$$e^{i\phi(t)} d = (\gamma^t/\gamma) \left[e^{-iEt} + r \right] \tag{115}$$

where we have used the notation $\dot{r} = \partial_t r(t, E)$. This set of linear equations can be formally integrated and one obtains the correction to the wide band limit. For $\gamma_t = \gamma$, we get,

$$\dot{r} - i(E + w(t)/2) r = ie^{-iEt} w(t)/2. \tag{116}$$

Assuming that the voltage is small compared to E, we can neglect $w(t)$ in the left hand side of Eq. (116) and obtain

$$r(E', E) = -\frac{w(E' - E)}{E' + E} + O[w(E)/E]^2 \tag{117}$$

where $w(E)$ is the Fourier transform of the voltage pulse $w(t)$, or equivalently,

$$r(t, E) = \frac{i}{2} \int_{-\infty}^{t} du e^{-i2Eu + iEt} w(u) \tag{118}$$

and

$$d(t, E) = e^{-i\phi(t) - iEt} + \frac{i}{2} e^{-i\phi(t)} \int_{-\infty}^{t} du e^{-i2Eu + iEt} w(u). \tag{119}$$

It is interesting to look at Eq. (119) for a time larger than the total duration of the pulse, so that the integral of the right hand side is simply $w(-2E)$. We get,

$$d(t, E) = e^{-i\phi(t) - iEt} \left[1 + \frac{i}{2} w(-2E) e^{i2Et} \right] + O[w(E)/E]^2. \tag{120}$$

We find that the first correction to the wide band limit corresponds to a beating of frequency $2E$. The corresponding term is, however, very small as $w(\epsilon)$ vanishes when ϵ is larger than $\max(V_P, \hbar/\tau_P)$ which, under the assumptions of the wide band limit, is much smaller than E_F.

9.2. Scattering matrix: numerics

As a test of the consistency of our different approaches, Fig. 10 shows the transmission probability $d(E', E)$ of the one dimensional chain as obtained from a numerical calculation [WF-D method followed by the generalized Fisher–Lee formula

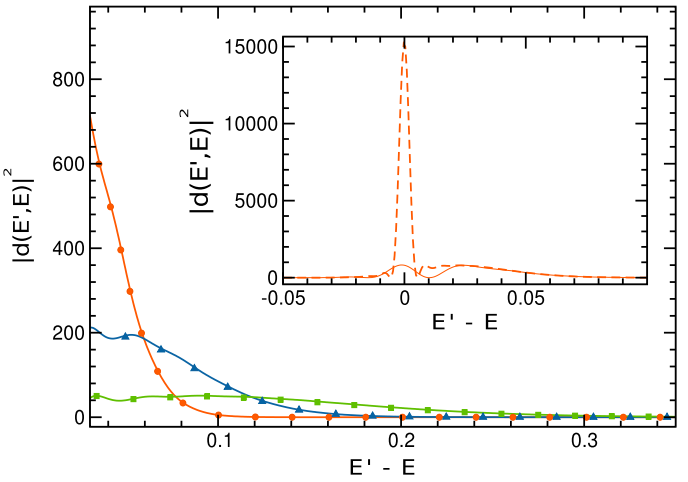

Fig. 10. Transmission probability of an incoming particle at energy $E = -1\gamma$ for a Gaussian voltage pulse $w(t) = V_P e^{-4\log(2)t^2/\tau_P^2}$ with amplitude V_P, width τ_P and fixed product $V_P\tau_P = 5.9$. Full lines corresponds to Eq. (91) while symbols are numerical results. Orange circles : $V_P = 0.059\gamma$, $\tau_P = 100\gamma^{-1}$, blue triangles: $V_P = 0.118\gamma$, $\tau_P = 50\gamma^{-1}$, green squares: $V_P = 0.236\gamma$, $\tau_P = 25\gamma^{-1}$. Inset: convergence of the discrete Fourier transform for two different values of t_M (same parameters as the orange circles). (For interpretation of the references to color in this figure legend, the reader is referred to the web version of this article.)

Eq. (47)] and the analytical result $d(E', E) = K^*(E-E')$ in the wide band limit [Eq. (91), the Fourier transform was performed numerically]. First, we find that the wide band limit gives excellent results; the analytics match the numerical results even for pulses that are quite large in energy (V_P up to 20% of the injected energy E). Second, we find that, as expected, the characteristic energy for the decay of $d(E', E)$ is indeed given by $\max(V_P, \hbar/\tau_P)$. Last, we find (inset) a large peak of width $\hbar/t_M$ and height $t_M/\hbar$ around $E' = E$. This peak, which converges to $\delta(E' - E)$ when $t_M \to \infty$ corresponds to the fact that for most of the time there is no time-varying voltage in the system which is therefore elastic. This can also be seen from the analytical expression of $K(E)$, which can be obtained in the case of a Lorentzian pulse [30]. Indeed for $w(t) = \frac{2\tau_P}{\tau_P^2+t^2}$, one obtains,

$$e^{i\phi(t)} = \frac{t - i\tau_P}{t + i\tau_P} \quad \text{and} \quad K(E) = 2\pi\delta(E) - 4\pi\,\tau_P e^{E\tau_P}\theta(-E). \tag{121}$$

9.3. Spreading of a voltage pulse inside a one dimensional wire: analytics

Going beyond the linear dispersion to study the spreading of the voltage pulse is not straightforward using the above wave matching method; we now take a different approach. We consider a pulse whose duration τ_P is short with respect to the total propagation time that will be considered, yet long with respect to $\hbar/E$. At a small time t_0 just after the pulse we can safely ignore the spreading of the pulse and the wave function is given by

$$\psi(x, t_0) = \frac{1}{\sqrt{v}} e^{-i\phi(-x/v)} e^{-iEt_0} e^{ikx} \tag{122}$$

Eq. (122) will be used as our initial condition. As noticed before, the voltage pulse takes the form of a phase domain wall that modifies the existing plane wave, as the function $\phi(-x/v)$ is constant except within a small window of size $v\tau_P$. We now introduce explicitly the modulation of the plane wave $Y(x, t)$,

$$\psi(x, t) = \frac{1}{\sqrt{v}} Y(x, t) e^{-iEt+ikx} \tag{123}$$

$Y(x, t)$ verifies $Y(x, t_0) = e^{-i\phi(-x/v)}$. To obtain the evolution of $Y(x, t)$ for times $t > t_0$, we inject the definition of the wave function Eq. (123) into the (free) Schrödinger equation and obtain,

$$i\partial_t Y(X, t) = -\frac{1}{2m^*}\Delta_X Y(X, t) \tag{124}$$

where the Laplacian $\Delta_X = \partial_{XX}$ acts on the coordinate $X = x - vt$ which follows the ballistic motion of the pulse. Solving this free Schrödinger equation is now straightforward and one proceeds as for a "regular" wave packet. In momentum space we have

$$Y(X, t) = \int \frac{dQ}{2\pi} e^{-iQX} e^{-iQ^2 t/(2m^*)} Y(Q, t = 0) \tag{125}$$

with

$$Y(Q, t = 0) = vK^*(Qv). \tag{126}$$

In a few cases one knows $K(E)$ explicitly and one an explicit formula for the wave function can be obtained. In the case of a Lorentzian pulse $K(E)$ is given by Eq. (121) and the integration in Eq. (125) provides an explicit expression,

$$Y(X, t) = 1 - v\tau_P\sqrt{\frac{2m^*\pi}{it}}\exp\left(\frac{m^*(iX - v\tau_P)^2}{2it}\right)\left[1 + \mathrm{Erf}\left(\frac{iX - v\tau_P}{2\sqrt{it/(2m^*)}}\right)\right] \tag{127}$$

with the usual definition of the error function $\mathrm{Erf}(x) = (2/\sqrt{\pi})\int_0^x e^{-x^2}dx$.

9.4. Spreading of a voltage pulse inside a one dimensional wire: numerics

The previous form of $Y(x, t)$ is the voltage pulse analogue of the spreading of a wave packet. It can be recast as a function of the dimensionless position $\bar{X} = X/(v\tau_P)$ and time $\bar{t} = t/[m^*(v\tau_P)^2]$. The typical spreading takes place "diffusively", i.e. $\Delta\bar{X} \propto \sqrt{\bar{t}}$, as for a regular wave packet. However, the peculiarity of the voltage pulse (i.e. it is merely a localized deformation of the *phase* of an existing stationary wave rather than the modulation of its amplitude) manifests itself in the presence of oscillations in the charge density. Fig. 11 shows the calculation of the local charge density

$$\rho_E(x, t) = |\Psi_E(x, t)|^2 \tag{128}$$

obtained from numerical calculations (left panels) and from Eq. (127) (upper right panel). The two upper color plots provide the same quantity as calculated numerically (left) and analytically (right). We find that the analytical description is fairly accurate despite various possible sources of discrepancy. The numerics are performed with our tight-binding model which slightly deviates from the continuum and the analytics neglect the quadratic dispersion at small times. A more detailed comparison is shown in Fig. 11(d) where we have plotted a cut at fixed x of the local charge density. The lower left plot corresponds to a different (Gaussian) form of the pulse from which a close analytical expression could not be obtained.

The most striking feature of the "spreading of the voltage pulse" is the appearance of density oscillations which are reminiscent of a wake. Although we could only analyze these oscillations analytically for the Lorentzian pulse, we actually found them for other shapes, the specificity of the Lorentzian pulse being that these oscillations always travel faster than the Fermi group velocity (the electrons' energy can only increase with a Lorentzian pulse, see Eq. (121)). Indeed for a Gaussian pulse (Fig. 11(c)), the oscillations also take place *after* the passage of the pulse.

At large time, Eq. (127) indicates that the amplitude of $\rho_E(x, t)$ scales as $1/\sqrt{\bar{t}}$ while the "period" of the oscillations increases as $\sqrt{\bar{t}}$. More precisely the nth extremum X_n of these oscillations obeys the relation,

$$X_n^2 = \frac{2\pi}{m^*}\left(n + \frac{1}{4}\right)t + (v\tau_P)^2. \tag{129}$$

In other words the positions X_n of the extrema increase diffusively with the quantum diffusion constant $D = h/m^*$. Fig. 12 shows the values of X_n as obtained numerically for a Gaussian or a Lorentzian pulse. We find (i) that the positions of the peaks in front of the pulse is not affected by the shape of the pulse (Lorentzian or Gaussian). Also (ii) the peaks behind the pulse (negative n, not present in the Lorentzian case) are positioned symmetrically with respect to the peaks with positive n.

In order to be able to observe these oscillations, one would need Dt to be larger than the original size of the pulse $v\tau_P$ which unfortunately happens to be very difficult. Indeed, one finds $D \approx 10^{-4}$–10^{-2} m^2 s^{-1} which translates into $X_1 \approx 1$ nm for a large propagation time $t = 10$ ns that would require, assuming $v \approx 10^4$ m s^{-1}, a 100 μm long coherent sample and $\tau_P < 100$ fs. This is clearly beyond available technology. In addition, the numerics and expressions obtained so far in this section refer to the contribution to the electronic density $\rho(x, t)$ at a given energy E. This contribution corresponds to the derivative of the corresponding density with respect to Fermi energy $d\rho(x, t)/dE_F = \rho_{E_F}(x, t)$. It can therefore be, in principle, directly measured by modulating the system with a uniform electrostatic gate, but its main interest lies in the physical insights it conveys. Fig. 13 shows full current (integrated over energy) as a function of space and time corresponding to the Gaussian pulse of Fig. 11(c). Beside the ballistic propagation of the pulse (at the Fermi velocity), one indeed observes that the oscillating tail survives the integration over energies. Note that these oscillations are reminiscent of other oscillations, associated with shock waves, that were predicted in [79–81]. In the latter case, a quantum wire was perturbed with a local density perturbation (as opposed to the voltage pulse studied here). However, as those oscillations also appear for a non-interacting gas and a finite curvature is needed to obtain them, they might be related to the present case.

The last figure of this section illustrates that our method is in no way limited to the simplest case of a ballistic one dimensional wire: higher dimensions, other lattices (e.g. graphene), or perturbations (polarized light, electrostatic gates) can be studied as well. Fig. 14 shows again a one dimensional wire, but a disordered region (Anderson model) has been placed between the sites $i = 1000$ and $i = 2000$ (dashed line). In this region, the on site energies ϵ_i are given by static random variables uniformly chosen between $[-W/2, W/2]$. These preliminary results show the propagation of a voltage pulse for

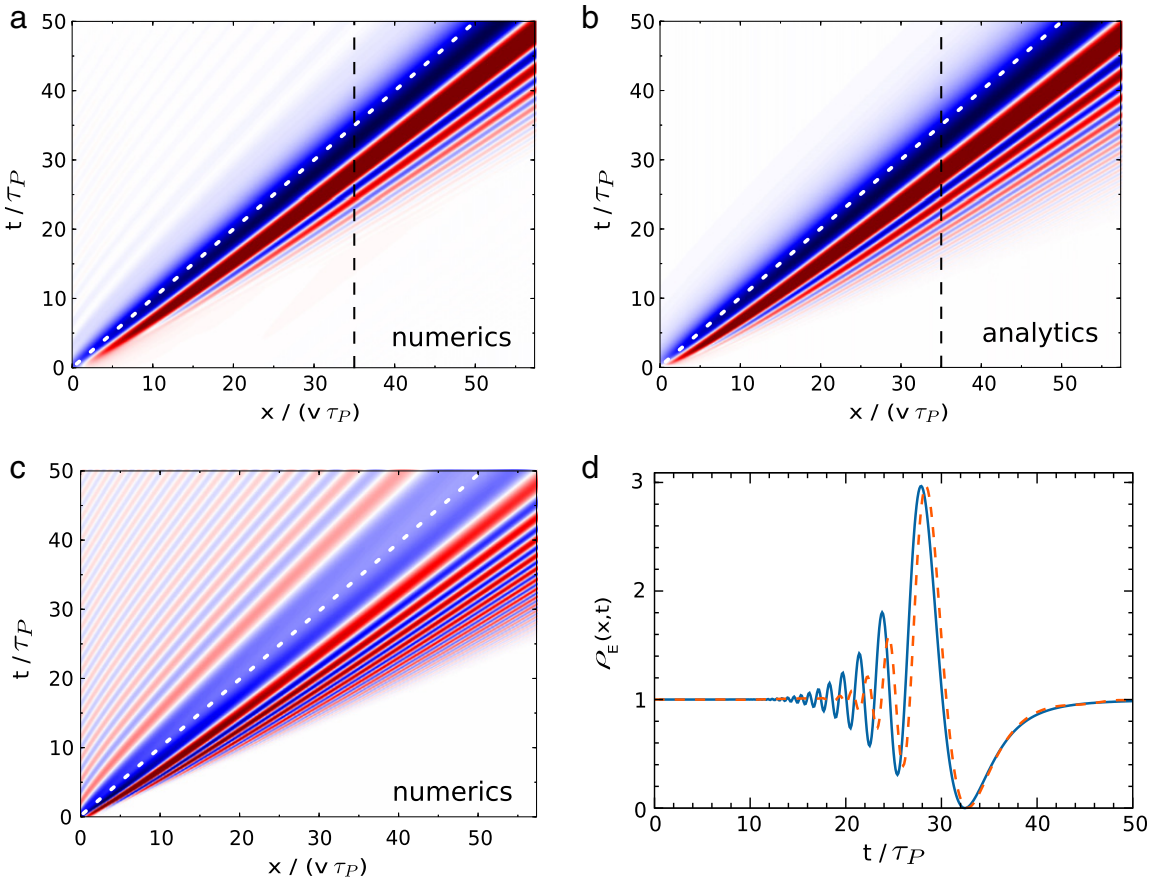

Fig. 11. Color plot of the local charge density $\rho_E(x,t)/\rho_E(x,t=0)$ as a function of space (in unit of $v\tau_P$) and time (in unit of τ_P) at energy $E=-1.8\gamma$ and $\tau_P=10\gamma^{-1}$. Levels of red (blue) correspond to local densities higher (lower) than one. The white dashed lines indicates the ballistic propagation $x=vt$. Panels (a) and (b) correspond to a Lorentzian pulse $w(t)=2\tau_P/(\tau_P^2+t^2)$ calculated analytically [right, Eq. (127)] and numerically [left]. Panel (c) shows the numerical result for a Gaussian pulse $w(t)=V_P e^{-4\log(2)t^2/\tau_P^2}$ with $V_P=0.59\gamma$. Panel (d) shows a cut at $x=35v\tau_P$ of the results of panel (a) (orange dashed line) and panel (b) (full blue line).

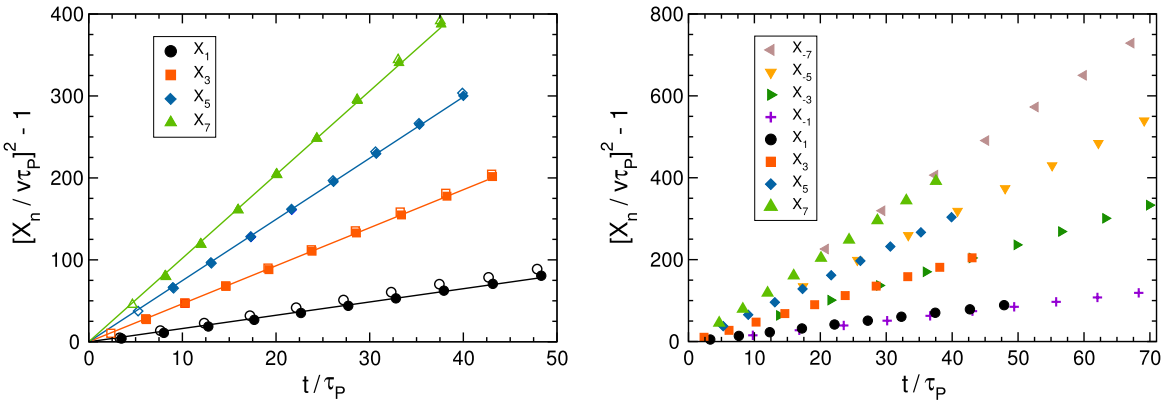

Fig. 12. Maxima of the oscillations appearing in Fig. 11(a) and Fig. 11(c) as a function of time. Left graph: full (empty) symbols correspond to the Lorentzian (Gaussian) pulse. Both cases are hardly distinguishable. Lines are linear fits of the numerical data obtained for the Lorentzian case. Right graph: all symbols correspond to the Gaussian pulse, negative (positive) values of n refer to maxima appearing before (after) the pulse.

different values of the width τ_P. The Anderson localization length ξ for this system is roughly equal to 400 sites ($\xi\approx 96/W^2$ at the center of the band) and we indeed find that after a set of multiple reflections, the transmitted current essentially

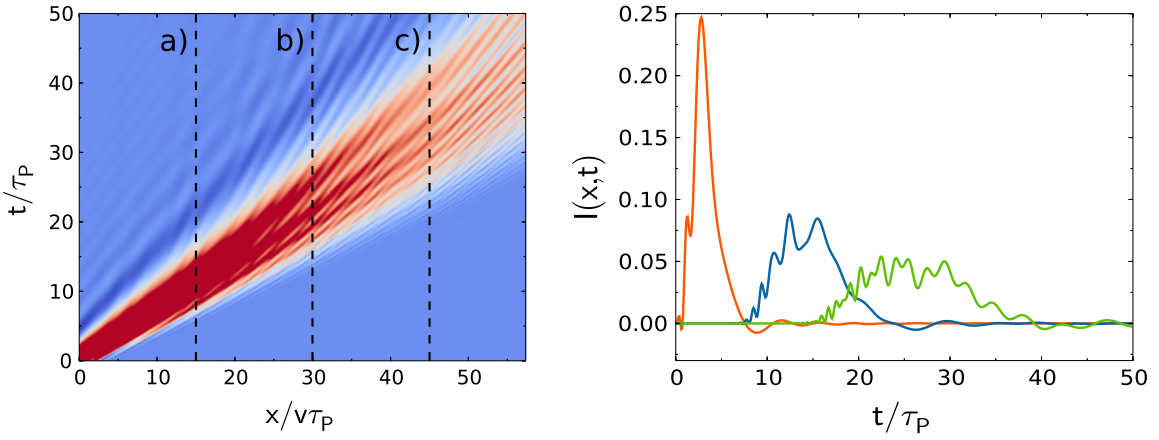

Fig. 13. Current density as a function of space (in unit of $v\tau_P$) and time (in unit of τ_P) for the Gaussian pulse of Fig. 11(c). Fermi level is set at $E_F = -1.8\gamma$. Left panel: the color map goes from zero values (blue) to 0.6 (red). Right panel: cut of the left panel at three positions in spaces (a), (b) and (c) corresponding to the three dashed lines shown on the left panel. Orange: $x = 15v\tau_P$, blue: $x = 30v\tau_P$, green: $x = 45v\tau_P$.

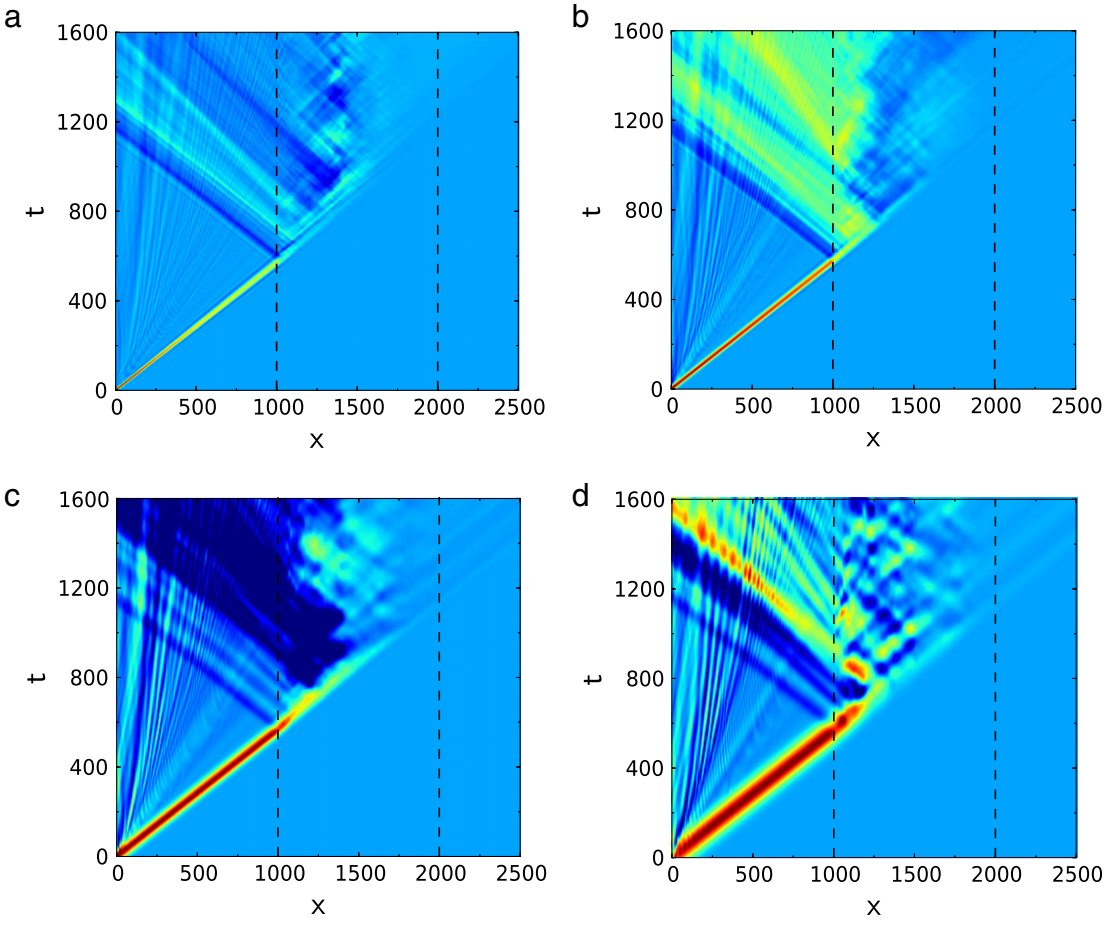

Fig. 14. Propagation of a Gaussian voltage pulse in a 1D quantum wire up to $t_{\max} = 1600\gamma^{-1}$. $E_F = -1\gamma$, $w(t) = V_P e^{-4\log(2)t^2/\tau_P^2}$ with $V_P = 0.05\gamma$ and $N = 2500$. A disordered region ($W = 0.5$) has been included between the two dashed lines (see text). The different color plots correspond to $\tau_P = 10\gamma^{-1}$ (a), $\tau_P = 20\gamma^{-1}$ (b), $\tau_P = 50\gamma^{-1}$ (c) and $\tau_P = 100\gamma^{-1}$ (d).

vanish after the middle of the disordered region. Further analysis would allow one to discuss the interplay between the duration of the pulse and the phenomena of Anderson localization. We differ such a step to a future publication.

10. A two dimensional application to a flying Qubit

We end this article by a simulation that goes beyond the one dimensional case studied so far. We will discuss an implementation of a solid state quantum bit known as a "flying Qubit" and directly inspired from recent experiments [5]. The results below are similar in spirit to those obtained earlier in [82], but the addition of the Fermi–Dirac statistic (taken into account here but not in [82]) allows one to make actual predictions for transport experiments. Our model system is sketched in Fig. 16. It consists of a large quasi-one dimensional wire of (width 2W) which is split in the middle by a top gate to which a depleting voltage V_T is applied. One effectively has two (weakly coupled) wires which form the two states of the flying Qubit (the up and down "states" correspond to the upper and lower wire respectively). The system has four terminals and we will compute the effective transmission probability of the wire into the up and down channel, i.e. the ratio between the total number of transmitted particle and the total number particles injected in the wire.

10.1. Integral over energies

Before going to the simulations of this device, let us briefly discuss the last technical difficulty that one is faced with when performing such simulations: the integral over incident energies. We have seen in Section 8 that only a small energy window around the Fermi level contributes to the transport properties and we would like now to understand how this fact manifests itself in the numerical calculations.

The central technical issue when performing the energy integral numerically is that within the WF method, one integrates over the injection energy E_{inj} (see Fig. 15 for a schematic). On the other hand, we have seen in Section 8 that in order to understand the various compensations that take place between the currents coming from different leads, we must add the contributions at a given energy E_{sys} (energy of the electron inside the mesoscopic region, i.e. after the pulse). This is illustrated in the upper right panel of Fig. 15: in case (A) the injected energy $E_{inj} < E_F$ is close enough to the Fermi energy that the voltage pulse can bring it to an energy $E_{sys} > E_F$ large enough for this contribution not to be compensated by electrons coming from the other side. In case (B) however, $E_{inj} \ll E_F$ so that $E_{sys} < E_F$ and all contributions are compensated by electrons injected from the right (at energy E_{sys}). Unfortunately, in the numerics we only control E_{inj} so that we cannot differentiate between case (A) and (B) and need to integrate over the whole energy range. This is not a real issue, however, as several tens of energy points are usually enough and these calculations can be performed in parallel. A real difficulty comes from case (C) where the injected energy E_{inj} is close to the bottom of the band so that after the pulse the electron can end up at a vanishing energy $E_{sys} = 0$ which results in a vanishing velocity. As a result these contributions get stuck at the place where the voltage drop takes place and cannot relax. This is illustrated on the left panel of Fig. 15 where we have plotted the current flowing through the device as a function of t and E_{inj}. We find indeed that contributions that are too close to the bottom of the band relax extremely slowly (by too close we mean closer than $\max(V_P, \hbar/\tau_P)$). This makes numerical convergence difficult as one needs very long simulation time to recover particle conservation.

Our strategy to remove the effect of those contributions is to improve our model of the electrodes. In actual experimental setups the electrodes are essentially metallic (high Fermi energy) so that the contributions corresponding to case (C) are essentially negligible. We therefore add an external potential which is vanishing in the mesoscopic system and negative in the electrode, as seen in the lower part of Fig. 15. As the current is measured in the region where this potential vanishes (i.e. on the right in Fig. 15), the very low injected energies (case C) will not contribute to the current any more and one recovers particle conservation even for rather small simulation times.

10.2. Model

We consider the device sketched Fig. 16 for an electronic density of $n_s = 0.3\ 10^{10}\ \mathrm{cm}^{-2}$ which corresponds, for a GaAs/GaAlAs heterostructure ($m^* = 0.069 m_e$), to $E_F = 108\ \mu\mathrm{eV}$ and $\lambda_F = 457\ \mathrm{nm}$ ($E_F = \hbar^2/(2m^*\lambda_F^2) = \hbar^2 \pi n_s/m^*$ with n_s being the full electron density including spins). The device half width is $W = 360$ nm and the length is $L = 10\ \mu\mathrm{m}$. We use Gaussian pulses $w(t) = eV_P e^{-4\log(2)t^2/\tau_P^2}$ with a width $\tau_P = 37$ ps and $V_P = 18\ \mu\mathrm{V}$. The total simulation time was $t_{\max} = 1.5$ ns with a time step $h_t = 3.7$ fs.

We use a simple one band Schrödinger equation that includes the confining potential $V(x, y, t)$ (due to the mesa and the gates).

$$i\hbar\partial_t \psi(x, y, t) = -\frac{\hbar^2}{2m^*}\Delta\psi(x, y, t) + V(x, y, t)\psi(x, y, t). \tag{130}$$

We rescale time in unit of the inverse of the Fermi energy $\tilde{t} = tE_F/\hbar$ and space in unit of the Fermi wave length $\tilde{x} = 2\pi x/\lambda_F$. The Fermi energy is rescaled to $\tilde{E}_F = 1$, and we get the dimensionless Schrodinger equation,

$$i\partial_{\tilde{t}}\psi(\tilde{x}, \tilde{y}, t) = -\tilde{\Delta}\psi(\tilde{x}, \tilde{y}, \tilde{t}) + [V(\tilde{x}, \tilde{y}, \tilde{t})/E_F]\psi(\tilde{x}, \tilde{y}, \tilde{t}). \tag{131}$$

The confining potential includes, in particular, the contribution from the tunneling gate $V_T(x, y, t) = V_T(t)\delta(y)$, the other gates being always static. For actual simulations, the model is discretized on a square lattice with lattice constant a and we

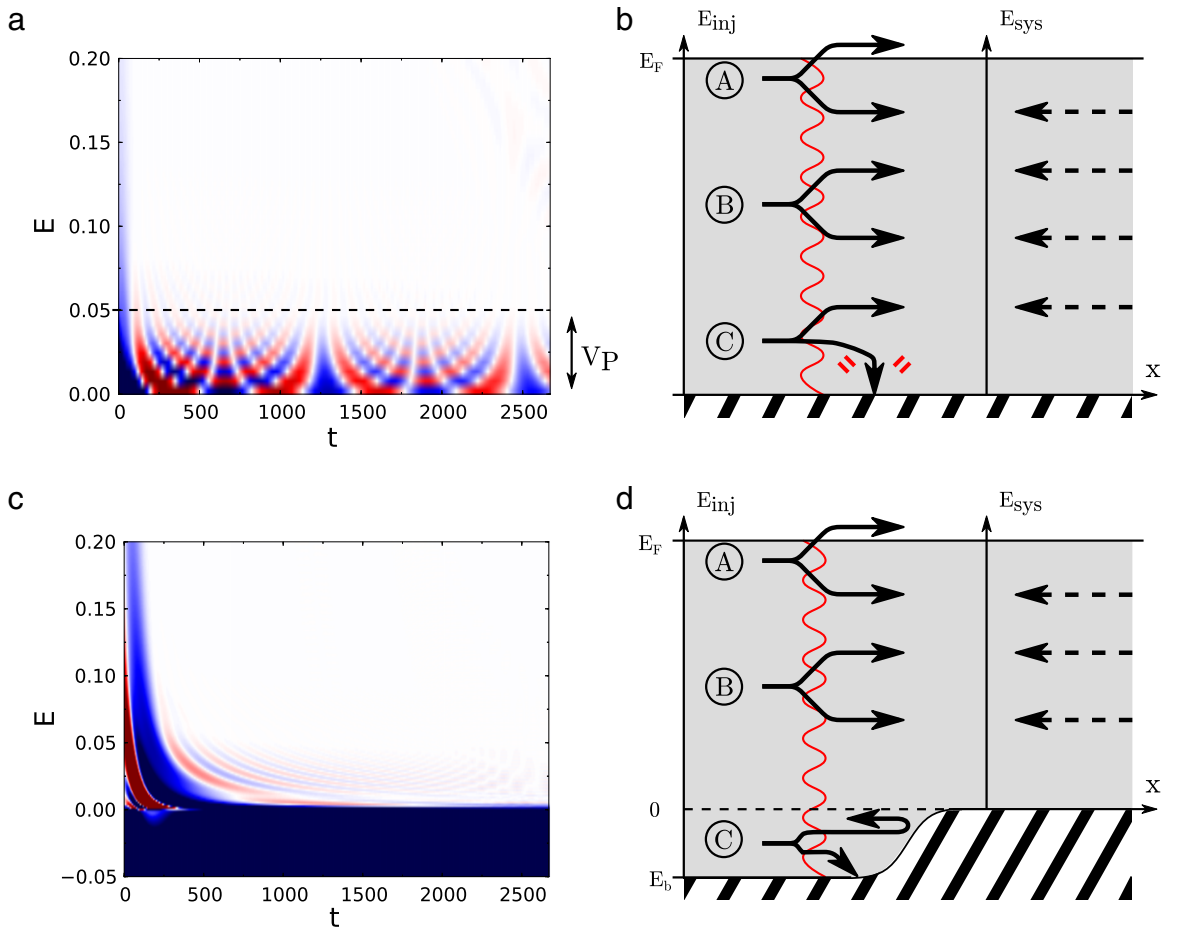

Fig. 15. Left panels: contribution $I(E,t)$ to the current $I(t)$ as a function of the injected energy E and time t. The system is a one dimensional wire where one send a Gaussian pulse, $V(t) = V_P e^{-4\log(2)t^2/\tau_P^2}$, with width $\tau_P = 100\gamma^{-1}$ and amplitude $V_P = 0.05\gamma$. Red (blue) indicates values above (below) one. Right panels: Schematic of the various contributions coming from different energies: Case A: the injected energy E_{inj} is close to the Fermi energy E_F. Case B: the injected energy E_{inj} is well below E_F (these terms eventually give a vanishing contribution). Case C: the injected energy E_{inj} is close to the bottom of the band. These terms also give a vanishing contribution but they relax extremely slowly with time. Lower panels: same as the upper panels but including our energy filtering scheme which removes the contributions from case C.

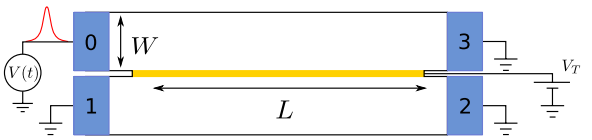

Fig. 16. Sketch of our flying Qubit consisting of two wires of width W connected to four leads (blue). The wires are coupled via a tunneling gate V_T with length L (yellow). Particles are injected by means of a voltage pulse which acts as the initial condition of the problem. (For interpretation of the references to color in this figure legend, the reader is referred to the web version of this article.)

introduce $\psi_{n_x,n_y}(\tilde{t}) \equiv \psi(n_x a, n_y a, \tilde{t})$. The discretized Schrödinger equation reads,

$$i\partial_{\tilde{t}}\psi_{n_x,n_y} = -\gamma[\psi_{n_x+1,n_y} + \psi_{n_x-1,n_y} + \psi_{n_x,n_y+1} + \psi_{n_x,n_y-1} - 4\psi_{n_x,n_y}] + V_{n_x,n_y}(\tilde{t})\psi_{n_x,n_y} \tag{132}$$

where $\gamma = 1/a^2$. Note that $V_T(\tilde{x},\tilde{y},\tilde{t})$ is discretized into $[V_T]_{n_x,n_y}(\tilde{t}) = (V_T(\tilde{t})/a)\delta_{n_y,0}$.

10.3. Time-resolved simulations

Let us now discuss the results of the simulations. Fig. 17 shows the total number of transmitted particles in the upper (lead 3, $n_\uparrow$) and lower (lead 2, $n_\downarrow$) channels as a result of the voltage pulse sent in the upper electrode (lead 0). We find that these numbers oscillate as a function of the tunneling gate voltage V_T which demonstrates that it is possible to dynamically

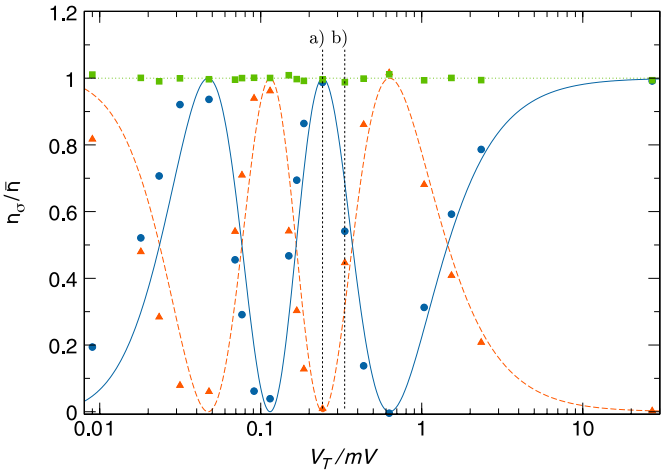

Fig. 17. The number of transmitted particles through lead 2 (orange triangles) and lead 3 (blue circles) ($n_\downarrow$ and $n_\uparrow$, collectively n_σ) normalized by the number of injected particles in lead 0 ($\bar{n}$) as a function of the tunneling gate potential, V_T. The green squares are the sum $n_\downarrow + n_\uparrow$. The corresponding lines are the DC transmission probabilities of the system between leads 0&2 (dashed orange) and 0&3 (full blue) and their sum (dotted green). The values of V_T indicated by the black dashed lines labeled (a) and (b) correspond to the values of V_T used to produce Fig. 18. These results were produced with a Gaussian voltage pulse as described in the main text. (For interpretation of the references to color in this figure legend, the reader is referred to the web version of this article.)

control the superposition of the wave function into the upper and lower part of the leads. In the DC limit, one expects $n_\uparrow = \bar{n}\cos^2[(k_A - k_S)L]$ ($n_\downarrow = \bar{n}\sin^2[(k_A - k_S)L]$) where $\bar{n}$ is the total number of electrons sent by the pulse and k_A (k_S) is the momentum of the antisymmetric (symmetric) mode in the wire. We find a good agreement between the simulations and the DC results, which is not trivial as we have worked in a fast regime where τ_P is smaller than the characteristic energy of the wire, $\hbar v_F(k_A - k_S)$ (in the adiabatic limit where τ_P is longer than all the characteristic times of the system, one should always recover the DC result). Indeed, Fig. 18 shows two snapshots of Fig. 17 for $V_T = 0.24$ mV and $V_T = 0.17$ mV. We find that the electronic density does oscillate, as a function of time, between the two arms of the flying Qubit. We find (case a) that at $t = 0.35$ ns the "pulse" is in a superposition of the up and down state while slightly later ($t = 0.5$ ns) the "pulse" is almost entirely in the lower arm. In the last simulation, shown in Fig. 19, we send the same pulse, wait for some time and abruptly raise the value of V_T to infinity (therefore effectively slicing the wire in two) at a time t_{cut}. From Fig. 18, one expects to observe oscillations of $n_\downarrow$ and $n_\uparrow$ as a function of t_{cut} and indeed Fig. 19 shows them. Note however that, in addition to "freezing" the system in one arm, the "slicing" operation also repels all the electrons beneath the tunneling gate. As a result several electrons (around 6 in our simulations) get expelled from the system. Fig. 19 is obtained by performing two simulations, one with the pulse and one without, and subtracting the two results in order to cancel out this spurious effect.

The device of Fig. 16 contains, in fact, quite rich physics but we shall end our discussion here. The purpose was to show that the formalism introduced in this article allows one to perform simulations on models and time scales large enough to be meaningful for mesoscopic physics. Further discussions of the physics involved in actual devices will be conducted elsewhere.

11. Conclusion

In the first part of this paper we have shown the equivalence between three different theoretical approaches of time-dependent nanoelectronics: the NEGF formalism, the Scattering approach and the partition-free initial condition approach. Building on these different theories, we have developed various strategies to perform numerical simulations for those systems. We eventually converged to a very simple algorithm (WF-D) whose performance is many orders of magnitudes better than a brute force integration of the NEGF equations. Systems with more than 10^5 sites with times long enough to probe their ballistic or even diffusive dynamics are now accessible to direct simulations. In the last part of this article, we have specialized the formalism to the particular case of voltage pulses. We found that the total number of transmitted particles is an observable that satisfies the basic requirements of a well behaved theory: particle conservation and gauge invariance. The article ends with two practical examples that illustrate our approach: a solid state equivalent of the spreading of the wave packet and an implementation of a "flying Qubit".

A strong emphasis was put on the technical aspects of time-dependent transport (and the corresponding simulations) with little room left for discussing the actual physics involved. We believe however that conceptually new physics will soon emerge from fast quantum electronics and that simulation methods, such as the one presented in this article, will play an important role in this development.

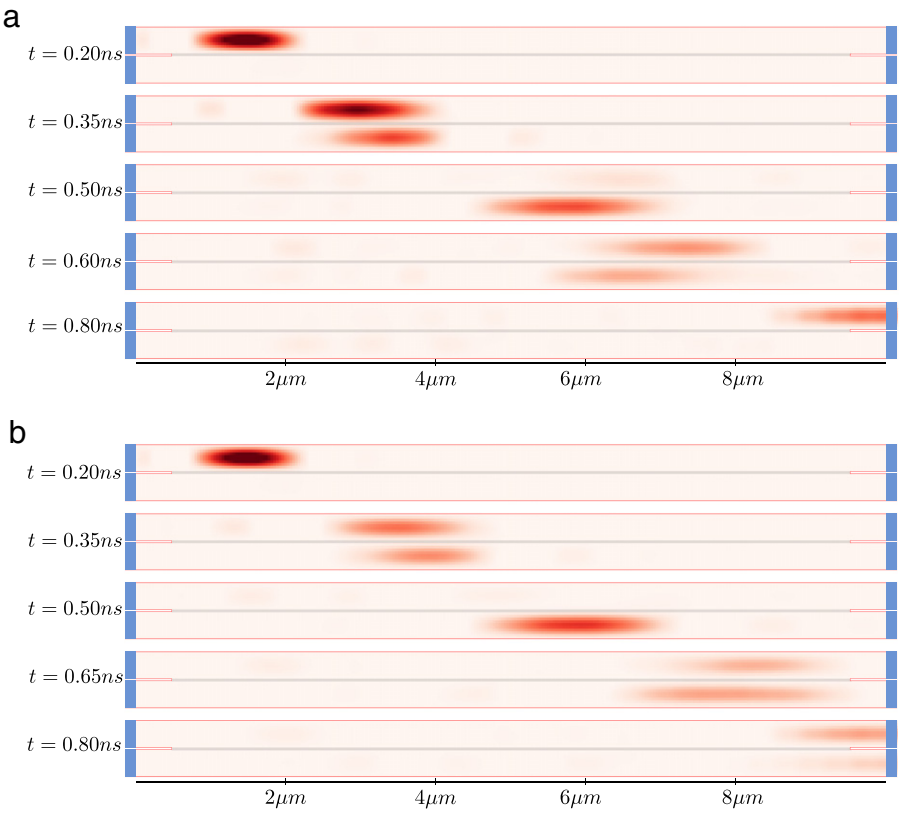

Fig. 18. Propagation of a voltage pulse within the coupled wire system. The figures show snapshots of the difference of the local charge density from equilibrium at different points in time. Figures (a) and (b) correspond to two different values of the tunneling gate voltage, 0.24 mV and 0.34 mV respectively. These results were produced with a Gaussian voltage pulse as described in the main text. Each of these two runs corresponds to a computing time per energy and per channel of 30 min on one computing core ($a = 0.5$, 7250 sites and 400000 time steps).

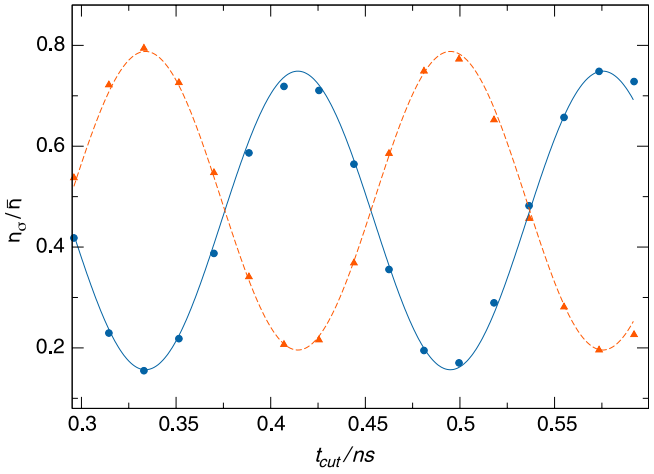

Fig. 19. The number of transmitted particles through lead 2 (orange triangles) and lead 3 (blue circles) ($n_\downarrow$ and $n_\uparrow$, collectively n_σ) normalized by the number of injected particles in lead 0 ($\bar{n}$) as a function of the time at which the coupling between the two wires of the flying Qubit system are cut, t_{cut}. The lines are cosine fits to the results from the numerics to guide the eye. These results were produced with a Gaussian voltage pulse as described in the main text.

Acknowledgments

The DC numerical simulations were performed with the Kwant software package, developed by C. W. Groth, M. Wimmer, A. R. Akhmerov and X. Waintal [70]. The simulations of Section 10 were performed with an implementation of WF-D which

is itself based on Kwant. Hence it shares all its general aspects (arbitrary dimension (1D, 2D, 3D), lattices (including say graphene), geometries (multiterminal) or internal structure (spins, superconductivity, spin–orbit, magnetic fields, etc.).

This work was supported by the ERC grant MesoQMC. MH also acknowledges the support from the French ANR grant (ANR-11-JS04-003-01).

Appendix A. Understanding the origin of the "source" term and "memory" kernel

As we have seen, there exist general connections between the various approaches used for (time-resolved) quantum transport (NEGF, scattering theory or the partition-free approach). As these connections were proved for a rather general class of problems (allowing for non trivial electrodes such as graphene as well as arbitrary time-dependent perturbations), the basic mathematical structure of these connections might be somewhat obscured. In this appendix, we consider the simplest situation where one can understand the origin of the "memory kernel" (term involving the self-energy) and "source" term that play a central role in our formalism: a simple one dimensional chain with just one electrode and no time-dependent perturbations.

Our starting point is the Schrödinger equation for the 1D chain in the energy domain,

$$\Psi_{x-1} + \Psi_{x+1} = E\Psi_x. \tag{A.1}$$

We suppose that the "system" corresponds to $x \geq 1$ (where one can possibly add terms such as $V_x\psi_x$ but those will be irrelevant for the present discussion) and the "electrode" corresponds to $x \leq 0$. As a boundary condition in the electrode, we impose the incoming part of the wave: for $x \leq 0$,

$$\Psi_x = e^{ikx} + re^{-ikx} \tag{A.2}$$

which in turn implies that $E = 2\cos k$. At this stage, we could proceed with "wave matching" and try to obtain an expression for the reflection amplitude r. Another possibility involves deriving an effective equation where r has disappeared, which amounts to finding the effective boundary condition imposed on the system due to the presence of the electrode. Writing the Schrödinger equation for $x = 0$ and $x = 1$ we get,

$$1 + r + \Psi_2 = E\Psi_1 \tag{A.3}$$

$$e^{-ik} + re^{ik} + \Psi_1 = E(1 + r). \tag{A.4}$$

Now using $E = e^{ik} + e^{-ik}$ we find,

$$[\Sigma^R\Psi_1 + i\Sigma^R v] + \Psi_2 = E\Psi_1 \tag{A.5}$$

where we have introduced the self-energy $\Sigma^R = e^{ik}$ and the velocity $v = \partial E/\partial k$. Eq. (A.5) is reminiscent of the original equation $\Psi_0 + \Psi_2 = E\Psi_1$. The value of the wave function in the electrode Ψ_0 has been replaced by an effective boundary condition and the electrodes effectively drop out of the problem. This effective boundary condition [first two terms in Eq. (A.5)] contains a self-energy term (proportional to Ψ_1) and a source term. This is in fact a generic consequence of the peculiar sort of boundary condition where we impose the incoming waves (as opposed to more conventional Dirichlet or Neumann boundary conditions). Upon transforming into the time domain, the self-energy term transforms into a convolution which gives rise to the memory kernel.

Let us now introduce an equation for a new wave function ψ_x which is defined for an infinite system,

$$\psi_{x-1} + \psi_{x+1} + \delta_{x,1}i\Sigma^R v = E\psi_x \tag{A.6}$$

such that for $x \leq 0$ one imposes the presence of outgoing modes only, i.e. ψ_x takes the form $\psi_x = re^{-ikx}$. Then, upon performing the same algebra as above, one finds that for $x \geq 1$, ψ_x satisfies Eq. (A.5). In other words, Ψ_x and ψ_x are equal for $x \geq 1$ even though the latter lacks the incoming part for $x \leq 0$. The generalization of these two wave functions corresponds directly to their equivalent as defined in the core of the text.

Appendix B. Derivation of the path integral formula (68)

The projection of Eq. (67) onto the central region $\bar{0}$ yields,

$$\forall\, u \in [t', t], \quad \mathcal{G}^R_{\bar{0}\bar{0}}(t, t') = i\mathcal{G}^R_{\bar{0}\bar{0}}(t, u)\mathcal{G}^R_{\bar{0}\bar{0}}(u, t') + i\sum_{i=1}^{M}\mathcal{G}^R_{\bar{0}\bar{i}}(t, u)\mathcal{G}^R_{\bar{i}\bar{0}}(u, t'). \tag{B.1}$$

We use the Dyson equation to rewrite $\mathcal{G}^R_{\bar{0}\bar{i}}(t, u)$ and $\mathcal{G}^R_{\bar{i}\bar{0}}(u, t')$ as follows:

$$\mathcal{G}^R_{\bar{0}\bar{i}}(t, u) = \int_u^t dv\, \mathcal{G}^R_{\bar{0}\bar{0}}(t, v)\mathbf{H}_{\bar{0}\bar{i}}(v)g^R_i(v, u)\mathcal{G}^R_{\bar{i}\bar{0}}(u, t') = \int_{t'}^u dv\, g^R_i(u, v)\mathbf{H}_{\bar{i}\bar{0}}(v)\mathcal{G}^R_{\bar{0}\bar{0}}(v, t'). \tag{B.2}$$

Lastly, we substitute these above relations into Eq. (B.1) and obtain,

$$\forall\, u \in [t', t], \quad G^R(t,t') = iG^R(t,u)G^R(u,t') + \sum_{i=1}^{M} \int_u^t dv\, G^R(t,v) \int_{t'}^u du\, \mathbf{H}_{\bar{0}\bar{i}}(v) g_{\bar{i}}^R(v,v') \mathbf{H}_{\bar{i}\bar{0}}(v') G^R(v',t') \tag{B.3}$$

which is essentially Eq. (68).

Appendix C. Various analytical results for Green's functions of the 1d chain

We gather here a few analytical results for the 1d chain that were used to benchmark the numerical results shown in this work. Given an analytic function f our convention for Fourier transforms is

$$f(t) = \int \frac{dE}{2\pi} f(E) e^{-iEt} \tag{C.1}$$

$$f(E) = \int dt\, f(t) e^{iEt}. \tag{C.2}$$

The expressions below correspond to the Hamiltonian (62) for the perfect one dimensional chain ($\epsilon_i = 0$). The Lesser Green's functions were computed at zero temperature with $E_F = 0$. Energies are written in units of the hopping parameter γ, and times are in units of γ^{-1}.

- We begin with self-energies in energy for a semi-infinite lead,

$$\Sigma^R(E) = \begin{cases} \frac{E}{2} - i\sqrt{1 - \left(\frac{E}{2}\right)^2} & \text{if } |E| \le 2 \\ \frac{E}{2} - \sqrt{\left(\frac{E}{2}\right)^2 - 1} & \text{if } E > 2 \\ \frac{E}{2} + \sqrt{\left(\frac{E}{2}\right)^2 - 1} & \text{if } E < -2 \end{cases} \tag{C.3}$$

$$\Sigma^<(E) = \begin{cases} 2i\sqrt{1 - \left(\frac{E}{2}\right)^2} & \text{if } -2 \le E \le E_F \\ 0 & \text{else.} \end{cases} \tag{C.4}$$

- The corresponding Fourier transforms in time yields,

$$\Sigma^R(t) = -i\frac{J_1(2t)}{t}\theta(t) \tag{C.5}$$

$$\Sigma^<(t) = i\frac{J_1(2t)}{2t} - \frac{H_1(2t)}{2t} \tag{C.6}$$

  where J_n is the Bessel function of the first kind, and H_n is the Struve function of order n.
- We also computed Green's functions for the infinite 1d chain at equilibrium. The diagonal elements of the Retarded and Lesser Green's functions in energy read,

$$G_{xx}^R(E) = \begin{cases} \frac{1}{2i\sqrt{1 - \left(\frac{E}{2}\right)^2}} & \text{if } |E| \le 2 \\ \frac{1}{2\sqrt{\left(\frac{E}{2}\right)^2 - 1}} & \text{if } E > 2 \\ \frac{1}{-2\sqrt{\left(\frac{E}{2}\right)^2 - 1}} & \text{if } E < -2 \end{cases} \tag{C.7}$$

$$G_{xx}^<(E) = \begin{cases} \frac{i}{\sqrt{1 - \left(\frac{E}{2}\right)^2}} & \text{if } -2 \le E \le E_F \\ 0 & \text{else} \end{cases} \tag{C.8}$$

- and their counterparts in the time domain,

$$G^R_{xx}(t) = -iJ_0(2t)\theta(t) \tag{C.9}$$

$$G^<_{xx}(t) = \frac{i}{2}J_0(2t) - \frac{H_0(2t)}{2t}. \tag{C.10}$$

- The off diagonal element $G^<_{x,x+1}$ in energy and time domains read,

$$G^<_{x,x+1}(E) = \begin{cases} \dfrac{iE/2}{\sqrt{1-\left(\frac{E}{2}\right)^2}} & \text{if } -2 \le E \le E_F \\ 0 & \text{else} \end{cases} \tag{C.11}$$

$$G^<_{x,x+1}(t) = \frac{i}{2}J_0(2t) - \frac{1}{2}H_0(2t). \tag{C.12}$$

References

[1] N.S. Wingreen, A.-P. Jauho, Y. Meir, Time-dependent transport through a mesoscopic structure, Phys. Rev. B 48 (1993) 8487.
[2] Y. Blanter, M. Büttiker, Shot noise in mesoscopic conductors, Phys. Rep. 336 (2000) 1–166.
[3] M. Cini, Time-dependent approach to electron transport through junctions: general theory and simple applications, Phys. Rev. B 22 (1980) 5887–5899.
[4] S. Kurth, G. Stefanucci, A. Almbladh, C.-O. Rubio, E.K.U. Gross, Time-dependent quantum transport: a practical scheme using density functional theory, Phys. Rev. B 72 (2005) 035038.
[5] M. Yamamoto, S. Takada, C. Bauerle, K. Watanabe, A. Wieck, S. Tarucha, Electrical control of a solid-state flying qubit, Nature Nanotechnol. 7 (2012) 247.
[6] P.K. Tien, J.P. Gordon, Multiphoton process observed in the interaction of microwave fields with the tunneling between superconductor films, Phys. Rev. 129 (1963) 647–651.
[7] L.-H. Reydellet, P. Roche, D.C. Glattli, B. Etienne, Y. Jin, Quantum partition noise of photon-created electron–hole pairs, Phys. Rev. Lett. 90 (2003) 176803.
[8] K.K. Likharev, Dynamics of Josephson Junctions and Circuits, Gordon and Breach, New York, 1986.
[9] H. Pothier, P. Lafarge, C. Urbina, D. Esteve, M.H. Devoret, Single-electron pum based on charging effects, Europhys. Lett. 17 (1992) 249–254.
[10] P.W. Brouwer, Scattering approach to parametric pumping, Phys. Rev. B 58 (1998) R10135–R10138.
[11] F. Giazotto, P. Spathis, S. Roddaro, S. Biswas, F. Taddei, M. Governale, L. Sorba, A josephson quantum electron pump, Nat. Phys. 7 (2011) 857–861.
[12] M. Büttiker, H. Thomas, A. Prêtre, Mesoscopic capacitors, Phys. Lett. A 180 (1993) 364–369.
[13] M. Büttiker, A. Prêtre, H. Thomas, Admittance of small conductors, Phys. Rev. Lett. 71 (1993) 465.
[14] M. Buttiker, Capacitance, admittance, and rectification properties of small conductors, J. Phys.: Condens. Matter 5 (1993) 9361.
[15] M. Büttiker, A. Prêtre, H. Thomas, Dynamic conductance and the scattering matrix of small conductors, Phys. Rev. Lett. 70 (1993) 4114–4117.
[16] M. Büttiker, Time-dependent current partition in mesoscopic conductors, Il Nuovo Cimento 110B (1995) 509–522.
[17] J. Gabelli, G. Fève, J.-M. Berroir, B. Plaçais, A. Cavanna, B. Etienne, Y. Jin, D.C. Glattli, Violation of kirchhoff's laws for a coherent rc circuit, Science 313 (2006) 499.
[18] J. Gabelli, G. Fève, T. Kontos, J.-M. Berroir, B. Placais, D.C. Glattli, B. Etienne, Y. Jin, M. Büttiker, Relaxation time of a chiral quantum *r–l* circuit, Phys. Rev. Lett. 98 (2007) 166806.
[19] E. Zakka-Bajjani, J. Ségala, F. Portier, P. Roche, D.C. Glattli, A. Cavanna, Y. Jin, Experimental test of the high-frequency quantum shot noise theory in a quantum point contact, Phys. Rev. Lett. 99 (2007) 236803.
[20] E. Zakka-Bajjani, J. Dufouleur, N. Coulombel, P. Roche, D.C. Glattli, F. Portier, Experimental determination of the statistics of photons emitted by a tunnel junction, Phys. Rev. Lett. 104 (2010) 206802.
[21] J. Gabelli, B. Reulet, Shaping a time-dependent excitation to minimize the shot noise in a tunnel junction, Phys. Rev. B 87 (2013) 075403.
[22] M.V. Moskalets, Scattering Matrix Approach to Non-stationary Quantum Transport, Imperial College Press, London, 2012.
[23] O. Shevtsov, X. Waintal, Numerical toolkit for electronic quantum transport at finite frequency, Phys. Rev. B 87 (2013) 085304.
[24] B. Wang, J. Wang, H. Guo, Current plateaus of nonadiabatic charge pump: multiphoton assisted processes, Phys. Rev. B 68 (2003) 155326.
[25] F. Mahfouzi, J. Fabian, N. Nagaosa, B.K. Nikolić, Charge pumping by magnetization dynamics in magnetic and semimagnetic tunnel junctions with interfacial rashba or bulk extrinsic spin–orbit coupling, Phys. Rev. B 85 (2012) 054406.
[26] S.-H. Chen, C.-L. Chen, C.-R. Chang, F. Mahfouzi, Spin-charge conversion in a multiterminal aharonov-casher ring coupled to precessing ferromagnets: a charge-conserving floquet nonequilibrium green function approach, Phys. Rev. B 87 (2013) 045402.
[27] X. Oriols, D. Ferry, Quantum transport beyond dc, J. Comput. Electron. (2013).
[28] J. Cayssol, B. Dóra, F. Simon, R. Moessner, Floquet topological insulators, Phys. Status Solidi (RRL) - Rapid Research Lett. 7 (2013) 101–108.
[29] L.S. Levitov, H. Lee, G.B. Lesovik, Electron counting statistics and coherent states of electric current, J. Math. Phys. 37 (1996) 4845.
[30] J. Keeling, I. Klich, L.S. Levitov, Minimal excitation states of electrons in one-dimensional wires, Phys. Rev. Lett. 97 (2006) 116403.
[31] J. Dubois, J. Thibaut, C. Grenier, P. Degiovanni, P. Roulleau, D.C. Glattli, Private communication, 2013.
[32] J. Dubois, J. Thibaut, C. Grenier, P. Degiovanni, P. Roulleau, D.C. Glattli, Integer and fractional charge Lorentzian voltage pulses analyzed in the frame of Photon-assisted Shot Noise, ArXiv e-prints, 2012.
[33] G. Fève, A. Mahé, J.-M. Berroir, T. Kontos, B. Plaçais, D.C. Glattli, A. Cavanna, B. Etienne, Y. Jin, An on-demand coherent single-electron source, Science 316 (2007) 1169.
[34] A. Mahé, F.D. Parmentier, E. Bocquillon, J.-M. Berroir, D.C. Glattli, T. Kontos, B. Plaçais, G. Fève, A. Cavanna, Y. Jin, Current correlations of an on-demand single-electron emitter, Phys. Rev. B 82 (2010) 201309.
[35] F.D. Parmentier, E. Bocquillon, J.-M. Berroir, D.C. Glattli, B. Plaçais, G. Fève, M. Albert, C. Flindt, M. Büttiker, Current noise spectrum of a single-particle emitter: theory and experiment, Phys. Rev. B 85 (2012) 165438.
[36] Y. Sherkunov, N. d'Ambrumenil, P. Samuelsson, M. Büttiker, Optimal pumping of orbital entanglement with single-particle emitters, Phys. Rev. B 85 (2012) 081108.
[37] E. Bocquillon, F.D. Parmentier, C. Grenier, J.-M. Berroir, P. Degiovanni, D.C. Glattli, B. Plaçais, A. Cavanna, Y. Jin, G. Fève, Electron quantum optics: partitioning electrons one by one, Phys. Rev. Lett. 108 (2012) 196803.
[38] C. Grenier, R. Hervé, G. Fève, P. Degiovanni, Electron quantum optics in quantum hall edge channels, Modern Phys. Lett. B 25 (2011) 1053–1073.
[39] E. Bocquillon, V. Freulon, J.-M. Berroir, P. Degiovanni, B. Plaçais, A. Cavanna, Y. Jin, G. Fève, Coherence and indistinguishability of single electrons emitted by independent sources, Science 339 (2013) 1054–1057.
[40] J.D. Fletcher, M. Kataoka, H. Howe, M. Pepper, P. See, S.P. Giblin, J.P. Griffiths, G.A.C. Jones, I. Farrer, D.A. Ritchie, T.J.B.M. Janssen, Clock-controlled emission of single-electron wavepackets in a solid-state circuit, ArXiv e-prints, 2012.

[41] S. Hermelin, S. Takada, M. Yamamoto, S. Tarucha, A.D. Wieck, L. Saminadayar, C. Bauerle, T. Meunier, Electrons surfing on a sound wave as a platform for quantum optics with flying electrons, Nature 477 (2011) 435.
[42] R.P.G. McNeil, M. Kataoka, C.J.B. Ford, C.H.W. Barnes, D. Anderson, G.A.C. Jones, I. Farrer, D.A. Ritchie, On-demand single-electron transfer between distant quantum dots, Nature 477 (2011) 439.
[43] Z. Zhong, N. Gabor, J. Sharping, A. Gaetal, P. McEuen, Terahertz time-domain measurement of ballistic electron resonance in a single-walled carbon nanotube, Nature Nanotechnol. 3 (2008) 201.
[44] C. Caroli, R. Combescot, P. Nozieres, D. Saint-James, Direct calculation of the tunneling current, J. Phys. C 4 (1971) 916.
[45] L. Keldysh, Diagram technique for nonequilibrium processes, JETP 20 (1965) 1018.
[46] H.M. Pastawski, Classical and quantum transport from generalized Landauer–Büttiker equations. ii. time-dependent resonant tunneling, Phys. Rev. B 46 (1992) 4053–4070.
[47] A.-P. Jauho, N.S. Wingreen, Y. Meir, Time-dependent transport in interacting and noninteracting resonant-tunneling systems, Phys. Rev. B 50 (1994) 5528.
[48] Y. Meir, N.S. Wingreen, Landauer formula for the current through an interacting electron region, Phys. Rev. Lett. 68 (1992) 2512.
[49] Y. Zhu, J. Maciejko, T. Ji, H. Guo, J. Wang, Time-dependent quantum transport: Direct analysis in the time domain, Phys. Rev. B 71 (2005) 075317.
[50] E.C. Cuansing, G. Liang, Time-dependent quantum transport and power-law decay of the transient current in a nano-relay and nano-oscillator, J. Appl. Phys. 110 (2011) 083704.
[51] A. Prociuk, B.D. Dunietz, Modeling time-dependent current through electronic open channels using a mixed time-frequency solution to the electronic equations of motion, Phys. Rev. B 78 (2008) 165112.
[52] J. Maciejko, J. Wang, H. Guo, Time-dependent quantum transport far from equilibrium: an exact nonlinear response theory, Phys. Rev. B 74 (2006) 085324.
[53] A. Croy, U. Saalmann, Propagation scheme for nonequilibrium dynamics of electron transport in nanoscale devices, Phys. Rev. B 80 (2009) 245311.
[54] D. Hou, Y. He, X. Liu, J. Kang, J. Chen, R. Han, Time-dependent transport: time domain recursively solving negf technique, Physica E 31 (2006) 191.
[55] Y. Wei, J. Wang, Current conserving nonequilibrium ac transport theory, Phys. Rev. B 79 (19) (2009) 195315.
[56] D. Kienle, M. Vaidyanathan, F.m.c. Léonard, Self-consistent ac quantum transport using nonequilibrium Green functions, Phys. Rev. B 81 (11) (2010) 115455.
[57] Y. Wang, C.-Y. Yam, T. Frauenheim, G. Chen, T. Niehaus, An efficient method for quantum transport simulations in the time domain, Chemical Physics 391 (1) (2011) 69–77.
[58] J. Wang, Time-dependent quantum transport theory from non-equilibrium Green's function apprch, Journal of Computational Electronics 12 (3) (2013) 343–355.
[59] H. Xie, F. Jiang, H. Tian, X. Zheng, Y. Kwok, S. Chen, C. Yam, Y. Yan, G. Chen, Time-dependent quantum transport: an efficient method based on liouville-von-neumann equation for single-electron density matrix, J. Chem. Phys. 137 (2012) 044113.
[60] P. Bokes, F. Corsetti, R.W. Godby, Stroboscopic wave-packet description of nonequilibrium many-electron problems, Phys. Rev. Lett. 101 (2008) 046402.
[61] M. Konôpka, P. Bokes, Stroboscopic wave packet description of time-dependent currents through ring-shaped nanostructures, Eur. Phys. J. B 86 (2013) 1–15.
[62] G. Stefanucci, C.O. Almbladh, Time-dependent partition-free approach in resonant tunneling systems, Phys. Rev. B 69 (2004) 195318.
[63] E. Perfetto, G. Stefanucci, M. Cini, Time-dependent transport in graphene nanoribbons, Phys. Rev. B 82 (2010) 035446.
[64] G. Stefanucci, S. Kurth, A. Rubio, E.K.U. Gross, Time-dependent approach to electron pumping in open quantum systems, Phys. Rev. B 77 (2008) 075339.
[65] E. Khosravi, S. Kurth, G. Stefanucci, E.K.U. Gross, The role of bound states in time-dependent quantum transport, Appl. Phys. A 93 (2008) 355.
[66] J. Rammer, H. Smith, Quantum field-theoretical methods in transport theory of metals, Rev. Modern Phys. 58 (1986) 323.
[67] J. Rammer, Quantum Field Theory of Non-equilibrium States, Cambridge University Press, 2007.
[68] S. Datta, Electronic Transport in Mesoscopic Systems, Cambridge University Press, 1997.
[69] M. Wimmer, Quantum transport in nanostructures: from computational concepts to spintronics in graphene and magnetic tunnel junctions, Ph.D. thesis, Universität Regensburg, 2006.
[70] C.W. Groth, M. Wimmer, A.R. Akhmerov, X. Waintal, Kwant: a software package for quantum transport, 2013, ArXiv:1309.2926.
[71] I. Rungger, S. Sanvito, Algorithm for the construction of self-energies for electronic transport calculations based on singularity elimination and singular value decomposition, Phys. Rev. B 78 (2008) 035407.
[72] D.S. Fisher, P.A. Lee, Relation between conductivity and transmission matrix, Phys. Rev. B 23 (1981) 6851–6854.
[73] G. Stefanucci, R. van Leeuwen, Nonequilibrium Many-Body Theory of Quantum Systems: A Modern Introduction, Cambridge University Press, Cambridge, 2013.
[74] K. Kazymyrenko, X. Waintal, Knitting algorithm for calculating green functions in quantum systems, Phys. Rev. B 77 (2008) 115119.
[75] L.M. Delves, J.L. Mohamed, Computational Methods for Integral Equations, Cambridge University Press, 1988.
[76] S. Li, S. Ahmed, G. Klimeck, E. Darve, Computing entries of the inverse of a sparse matrix using the find algorithm, J. Comput. Phys. 227 (2008) 9408.
[77] D.E. Petersen, S. Li, K. Stokbro, H.H.B. Sørensen, P.C. Hansen, S. Skelboe, E. Darve, A hybrid method for the parallel computation of green's functions, J. Comput. Phys. 228 (2009) 5020–5039.
[78] M. Büttiker, Four-terminal phase-coherent conductance, Phys. Rev. Lett. 57 (1986) 1761–1764.
[79] E. Bettelheim, A.G. Abanov, P. Wiegmann, Nonlinear quantum shock waves in fractional quantum hall edge states, Phys. Rev. Lett. 97 (2006) 246401.
[80] E. Bettelheim, L. Glazman, Quantum ripples over a semiclassical shock, Phys. Rev. Lett. 109 (2012) 260602.
[81] I.V. Protopopov, D.B. Gutman, P. Schmitteckert, A.D. Mirlin, Dynamics of waves in one-dimensional electron systems: density oscillations driven by population inversion, Phys. Rev. B 87 (2013) 045112.
[82] A. Bertoni, P. Bordone, R. Brunetti, C. Jacoboni, S. Reggiani, Quantum logic gates based on coherent electron transport in quantum wires, Phys. Rev. Lett. 84 (2000) 5912–5915.